Inhibitor-wax interactions and PPD effect on wax crystallization: New approaches for GC/MS and NMR, and comparison with DSC, CPM, and rheometry

Jost Ruwoldt[1*], Geir Humborstad Sørland[1], Sébastien Simon[1], Hans-Jörg Oschmann[1], Johan Sjöblom[1]

[1]Ugelstad Laboratory, Department of Chemical Engineering, NTNU, N-7491 Trondheim, Norway

[*]Corresponding author e-mail: jost.ruwoldt@ntnu.no

Abstract

Three pour point depressants (PPDs) with different chemistries, and extracted asphaltenes were studied in their influence on wax crystallization in a model system. A new procedure for nuclear magnetic resonance (NMR) was developed to monitor changes in liquid phase as wax precipitated. Similar experiments were used to study *n*-alkane depletion during precipitation via the use of GC/MS. Additive performance was furthermore evaluated via differential scanning calorimetry (DSC), rheometry, and cross-polarized microscopy (CPM). All additives induced morphological changes to wax crystals, which also affected apparent viscosity and waxy gelling. Some additives improved flow-ability of the waxy model oil significantly, while others showed less pronounced or even adverse effects. Following DSC and NMR results, PPDs with good wax inhibition could delay both the onset of wax crystallization and reduce the amount of precipitated wax. In accordance with that, GC/MS showed additives to delay certain stages in compositional change during wax precipitation. Moreover, efficient PPDs could suppress interactions between liquid and solid waxes that showed in the NMR T_2-distribution. It appears that PPD beneficiation greatly influences the mobility of dissolved wax molecules, which would also entail an effect on interactions at the solid-liquid interface of wax crystals. In conclusion, experimental procedures for NMR and GC/MS were extended to study PPD-wax interactions more in-depth, and experimental results show potential for improving the knowledge of wax inhibition.

1. Introduction

Paraffin wax crystallization is one of the major challenges during crude oil production [1]. As the crude oil is transported through subsea pipelines, cooling of the oil induces wax crystallization once the wax appearance temperature (WAT) is reached. Issues associated with wax crystallization include increased fluid viscosity, formation of a wax deposition layer, pipeline restart issues due to waxy gelation, and reduced separation efficiency due to the formation of pickering emulsion [2]. Managing wax related issues entails significant costs, but if these issues are not addressed properly they can lead to production stop and even the loss of equipment [3-5]. Wax inhibitors play a central role in wax control, as these can ensure low fluid viscosity and prevent gelling. Even though the effect of these additives is well documented, the exact working mechanism remains still unknown [6, 7].

Wax crystallization as crystallization in general is reported to take place in three stages, which are (i) nucleation, (ii) growth, and (iii) agglomeration [8]. Stage (i) is usually delayed by a nucleation lag, which is cooling rate dependent [9]. The observed WAT or cloud point is therefore generally lower than the thermodynamic solubility limit of the wax. Wax crystal size increases during stage (ii), spawning crystal morphologies such as plates, needles, and malcrystalline masses [10]. Three dimensional interlocking can take place, marking wax crystal agglomeration of stage (iii). A solid like gel can be formed at a solid wax content as low as 1 – 2 % [11]. Upon shearing, this gel displays yielding behavior after an initial Hookean response, which is followed by gel breakage and degradation [12]. Gel yield strength is subject to thermal and shear histories [13], but also to the type of wax composition.

Macrocrystalline wax is reported to form high yield strength gels, whereas microcrystalline wax forms weak gels due to smaller and more compact crystal structures [14]. Macrocrystalline wax is mostly composed of low molecular weight *n*-alkanes (C_{16}-C_{40}), and microcrystalline wax contains large amounts of high molecular weight (~C_{40} and above) *iso*-alkanes and *cyclo*-alkanes [6].

Wax inhibitors include thermodynamic wax inhibitors, dispersants and surfactants, as well as pour point depressants (PPDs) [15]. Thermodynamic wax inhibitors are solvents or crude oil distillates that decrease WAT, but are deemed uneconomic due to a high volume required. Dispersants and surfactants act on the wax crystal surface, reducing particle-particle or particle-wall adhesion [15]. PPDs lower the pour point, which is defined as the temperature, at which the waxy oil loses its ability to flow freely [16]. PPDs are considered to predominantly act as crystal modifiers [7]. Crystal modifying substances alter wax crystal morphology via co-crystallization. During continued crystal growth, the incorporated PPD molecule can impose spatial hindrances to wax molecules that further precipitate on the crystal, leading to crystal distortion. This is often realised by polar moieties in the otherwise hydrocarbon-like polymer [17]. The hydrodynamic radius of wax crystals can thereby be reduced, as well as the propensity to overlap and form volume spanning networks. PPD polymers have also been reported to improve the thermodynamic solubility of wax via solute complexes [18]. Natural constituents of the crude oil can also act as PPD active substances. Asphaltenes have been confirmed as such by many authors [19-25]. It has been suggested that asphaltenes serve as nucleation site for wax crystallization, leading to more finely dispersed wax crystals [23, 24]. Moreover, co-precipitation mechanism for asphaltenes on wax crystals has been stated [21, 24, 26, 27]. Resins have also been mentioned as natural PPDs [28]. In addition, a recent study found that increasing the paraffin isomer content can affect wax crystallization in a beneficial way [29].

Industrial PPDs have been categorized into copolymers, comb polymers, and nanohybrid PPDs [6]. Copolymers usually consists of a polyethylene (PE) backbone that contains amorphous moieties with possibly higher polarity. Such chemistries include ethylene-propylene (PE-PEP), ethylene-butene (PE-PEB), poly(maleic anhydride amide co-a-olefin) (MAC), and ethylene-vinyl actetate copolymer (EVA) [30-33]. Comb polymers can be based on these, but additionally include pendant alkyl chains [6]. Ideally, such alkyl chains should match the average carbon number of the crude oil waxes [34]. Pendant alkyl chains and polar moieties can promote polymer interactions with wax and more polar components of the crude oil, such as asphaltenes [30, 34-37]. Nanoparticles and nanoparticle-polymer composites have been subject to recent studies, due to their ability to improve pour point beneficiation [38-45]. Such particles were stated to function as wax nucleation sites, which can lead to the formation of larger aggregates that are more compact and amorphous in structure [41, 43].

Aim and approach of this study are twofold. Firstly, improved procedures for NMR and GC/MS were presented to study PPD effect on wax crystallization in liquid phase. Similar approaches had been made by other authors in the past [46, 47], but involved procedures and techniques have been refined and extended since then. Secondly, experimental results from NMR and GC/MS technique were compared to established techniques, such as differential scanning calorimetry (DSC), rheometry, and cross-polarized microscopy (CPM). In addition, a comparison of wax precipitation curves (WPC) obtained by different techniques was made to better assess PPD effect on wax precipitation. Subject to the investigation were three polymeric PPDs and asphaltenes in a waxy model system. The goal was to evaluate the potential of new procedures for studying PPD-wax interactions and extend the knowledge about wax inhibition.

2. Experimental section

2.1. Materials

Solvents were obtained as toluene (anhydrous, 99.8%), deuterated toluene (anhydrous, 99.6 atom % Deut.), and *n*-heptane (anhydrous, 99%) from Sigmaaldrich, Norway. Asphaltenes were precipitated from a heavy crude oil (API 19°) originating from the Norwegian shelf by using *n*-hexane (HPLC grade, ≥97%) supplied by VWR, Norway. Characteristics and properties of these asphaltenes have been previously published [48-50]. Pour point depressants featured in this study are listed in Table 1. Macrocrystalline wax was obtained as 5405 Sasolwax from Sasol, Germany. A chromatogram of the wax is shown in Fig. 1. The wax consisted of mostly *n*-alkanes, where 84.6 wt% were in the range of *n*-C_{20} to *n*-C_{40} and 0.9 wt% were extrapolated to be *n*-C_{41} and higher. *Iso*-alkanes are visible as peaks in between larger *n*-alkane peaks, and the total isomer content was approximately 12 - 15 wt%. Standards for GC-analysis were purchased as heptadecane (analytical standard), and alkane standard mixture (C_{10}-C_{40}, even carbon numbers, 50 mg/l each in heptane) from Sigmaaldrich, Norway.

Table 1. Chemical additives

Alias	Chemistry based on	Supplied by
PPD A	polycarboxilate (proprietary)	BASF, Germany
PPD B	polyacrylate, EVA (proprietary)	BASF, Germany
PPD C	EVA, 40% vinyl acetate	DuPont, Germany
Asphaltenes	Asphaltenes from hexane precipitation of a heavy crude oil	-

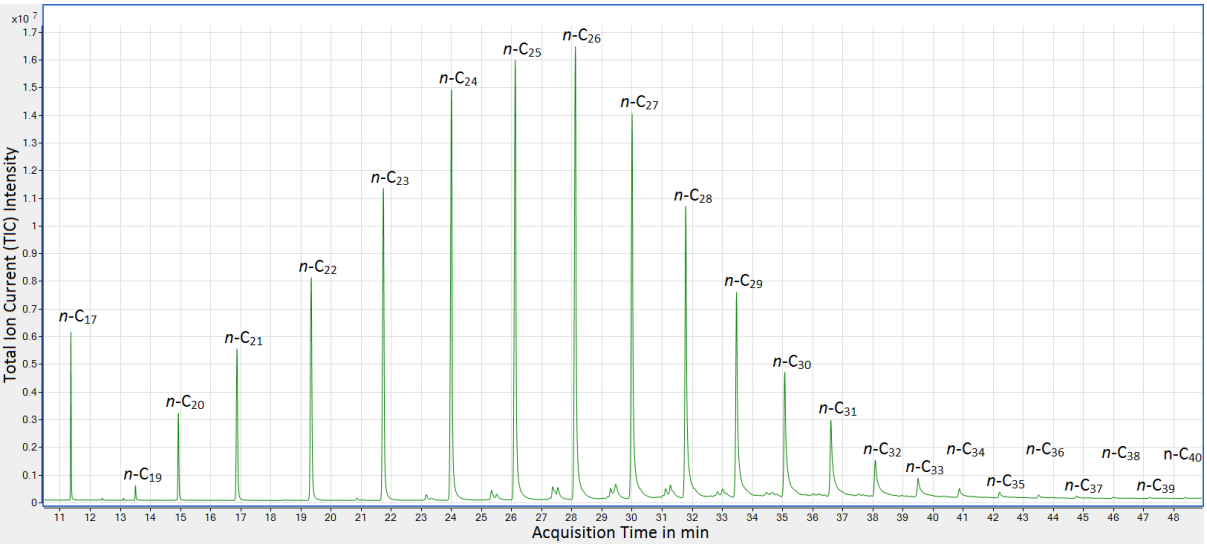

Fig. 1. TIC chromatogram of splitless injection of wax (Sasolwax 5405) in heptane with heptadecane (*n*-C_{17}) standard.

2.2. Sample preparation

The crude oil was heated to 60 °C for 1 h and shaken thoroughly before use, to ensure homogeneity of the sample. Asphaltenes were precipitated by diluting the crude oil sample with 40 ml *n*-hexane per gram crude oil and stirring overnight. The resulting mixture was then filtered through a 0.45 µm HVLP-type Millipore filter membrane and afterwards rinsed with *n*-hexane until the filtrate was clear. The yield of asphaltenes accounted for 2.3 wt% of the crude oil.

The samples PPD A and PPD B originally contained different petroleum cuts having 80 % and 50 % active content, respectively, according to manufacturer specifications. The polymers were solvent purified, after which a weight loss of 19.9 wt% (PPD A) and 48.0 wt% (PPD B) was recorded. The

purification procedure consisted of repeated addition and removal of toluene in a rotary evaporator at up to 90 °C and 200 mbar. The remaining substance was subsequently dried in an oven at 60 °C for 24 h under atmospheric pressure. To estimate any solvent remains in the polymeric PPD, samples were analyzed using a Q600 thermogravimetric analyzer (TGA). Heating the solid sample from 60 to 200 °C at a rate of 10 °C/min, the total weight loss amounted to 2.5 wt% for PPD A and 4.0 wt% for PPD B. Above 200 °C the weight loss increased rapidly as the polymer started to disintegrate. It was therefore concluded that the samples PPD A and PPD B consisted of mostly PPD active polymer with negligible traces of solvent.

Waxy samples, also referred to as model waxy oils, were prepared by first weighing the solids (PPD/asphaltenes and wax) and then adding the required amount of toluene. Wax was dissolved by heating to at least 20 °C above WAT for at least 30 min. PPD and asphaltene containing solutions were additionally sonicated prior to use. Sample concentrations of 1000 ppm PPD or asphaltenes and 5 wt% wax in toluene were consistently used for all types of experiments.

2.3. Differential scanning calorimetry (DSC)

DSC experiments were conducted on a Q2000 from TA Instruments. The instrument was calibrated by measuring the melting heat and temperature of pure indium and the calibration was verified by checking the melting temperature of pure water. For each experiment, 20 – 25 mg sample was loaded into Tzero Hermetic Aluminum Pans, which were sealed hermetically. The pans were weighed before and after the experiment, to ensure that no solvent loss had occurred. During each experiment run, the sample was first heated to 90 °C and then held isothermally for 10 min. A constant cooling rate of 0.2 °C/min was subsequently applied and data recording commenced. This heating program was repeated multiple times, as the reheating period showed to remove all thermal history.

WAT determination was conducted based on a previously published procedure [51]. In this procedure, the DSC heat flow with temperature is approximated by a straight line before wax crystallization onset. A confidence interval is calculated as 1.92 times the standard deviation of data from the straight line approximation. The WAT is then defined as the highest temperature, at which three consecutive points are outside of the confidence interval.

The WPC was computed from the excess heat, which is the difference of heat signal and interpolated baseline as shown in Fig. 2. The baseline was approximated as second degree polynomial of the specific heat capacity, as suggested by Coto et al [52]. This baseline approximation used data on a 10 K interval starting 5 °C above WAT, as well as data between -55 to -70 °C. The conversion between heat flow and specific heat capacity was done via equation (1), where c_p is the specific heat capacity, $\dot{Q}$ is the heat flow, C_r is the cooling rate, and K is an instrument calibration constant.

$$\dot{Q} = \frac{c_p C_r}{K} \tag{1}$$

The cumulative sum of excess heat (heat signal baseline subtracted from actual heat signal) could then be used to compute the amount of precipitated wax by dividing through the total sum of excess heat. The assumption of athermal behavior of the wax was thereby made, which implies that specific crystallization heat does not change with temperature, i.e. the excess heat is crystallizing mass are constantly proportional. An example for the determination of excess heat is given in Fig. 2. As can be seen, below -55 °C the heat signal has returned to a stable baseline. Computing the precipitated wax content via this intrinsic procedure was favored over procedures employing extrinsic properties, as the specific crystallization heat of wax was strongly affected by PPD addition.

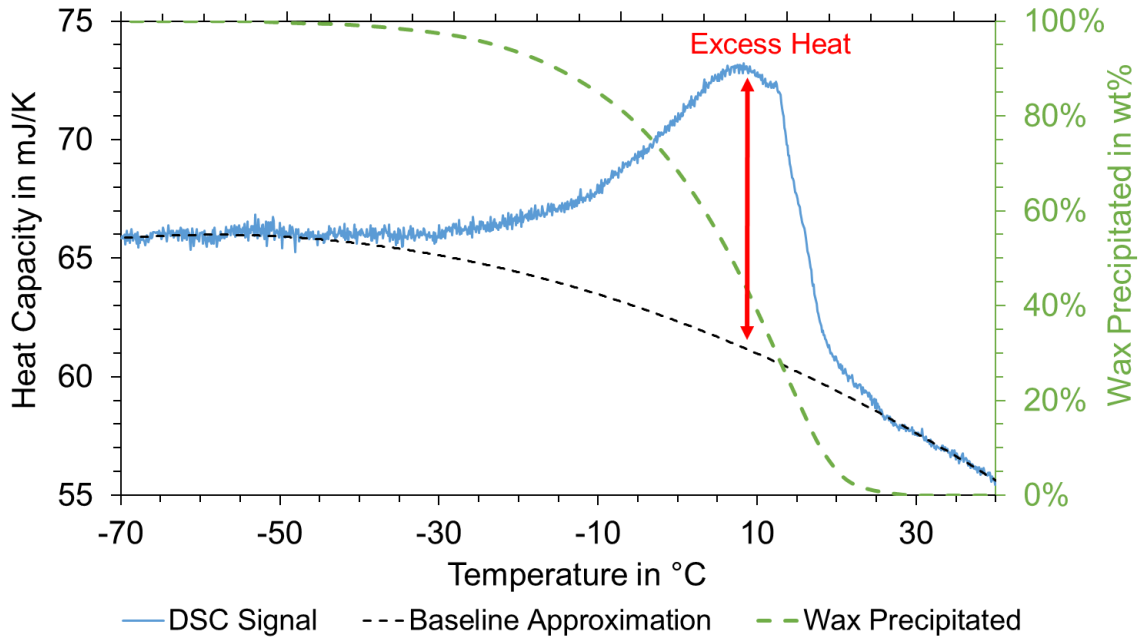

Fig. 2. WPC computation from DSC data of 5 wt% wax in toluene at a cooling rate of 0.2 °C/min. The heat flow represents the average of 4 measurements for improved signal to noise ratio at low cooling rates. The baseline was approximated by a 2nd degree polynomial.

2.4. Rheometry

Rheometric experiments were conducted on an Anton Paar Physica 301. The rheometer was equipped with a 4 cm diameter 2° cone and plate geometry, which had been sandblasted on both sides to provide additional roughness and to prevent slippage. The gap size was 0.170 mm. A solvent trap filled with toluene was used to prevent evaporation of the sample. The sample was loaded into the geometry, which had been preheated at 5 – 10 °C above WAT, after which cooling at a rate of 0.2 °C/min commenced.

In viscometry measurements a constant shear rate of 0.1 s^{-1} was applied. This shear rate is an order of magnitude lower than previous procedures used for WAT determination [51, 53, 54]. This was done, because the focus was not on WAT determination, but on monitoring viscosity changes due to wax crystallization. Higher shear rates and a consequently higher amount of total strain would have caused a higher degree of gel degradation, and thus lower measurement sensitivity.

Gel yield strength was measured by quiescently cooling to -2 °C, holding isothermally for 30 min, and then ramping the shearing from 10^{-4} – 1 s^{-1} logarithmically for 10 min. The yield strength was defined as the maximum shear stress recorded in the flow curve.

2.5. Cross polarized microscopy (CPM)

CPM imaging was done on a Nikon Eclipse ME600 microscope, which was fitted with cross-polarization filter and a CoolSNAP-Pro camera by Media Cybernetics. Temperature control was handled by a Linkham PE 94 and LTS-120E Peltier system. The preheated samples were filled into glass capillaries with a cross section of 0.3 x 0.03 mm, which were sealed on both ends using 3 M Scotch cyanoacrylate glue and fixed in place on microscope slides. To prevent sample contamination, an air bubble was kept on both ends of the capillary. During measurements, the temperature was first ramped to 60 °C, kept isothermally for 15 min, cooled to 30 °C at a rate of 10 °C/min, and then cooled

to -2 °C at a rate of 0.2 °C/min. The temperature was held constant at -2 °C and imaging was done within the time frame of 30 – 60 min of the isothermal period.

2.6. Nuclear Magnetic Resonance (NMR)

NMR Experiments were conducted on a low field (21 MHz) NMR spectrometer without frequency resolution, which was supplied by Anvendt Teknologi AS, Norway. The sequence applied was the standard Carr-Purcell-Meiboom-Gill (CPMG) sequence for acquiring the transverse relaxation time (T_2) decay [55]. The inter echo spacing (2τ) used was 300 μs and the number of echoes acquired was set to 12000. To produce the T_2-distributions from the multi-exponentially decaying curve, the one-dimensional Inverse Laplace Transform was made use of [56]. T_2-distributions were used as a qualitative and quantitative measure, as solids are known to display short T_2, whereas substances in the liquid state show long T_2. To quantify substances in the liquid state, a signal intensity was computed as sum over $T_2 > 3 \cdot 10^{-3}$ s by convention.

All experiments used a constant sample weight of 3 g. Deuterated toluene was used as bulk solvent to obtain T_2-distributions that reflect only the dissolved components. The molecular weight of deuterated toluene was taken into account in the weighing procedure, to mimic the same mole fraction of experiments with 5 wt% wax in non-deuterated toluene. The temperature ramping started with an isothermal segment at 45 °C in the beginning, and then cooling at a rate of 0.2 °C/min took place. Sample temperature was controlled with preheated or precooled air that continuously flushed the vial from bottom to top. The flow of air was held constant throughout all experiments by applying constant inlet pressure. As determining the actual sample temperature inside the NMR is difficult, an apparent temperature was computed from comparing dynamic and static experiments with 5 wt% hexadecane in deuterated toluene. Dynamic experiments refer to applying a constant cooling rate of 0.2 °C/min, whereas in static experiments the sample was equilibrated isothermally for 60 min before data acquisition. The data was then used to compute a temperature correction function, as shown in Fig. 3. This was done by fitting static and dynamic data with a polynomial function each, and computing the difference. The obtained function accounts for the gap between setpoint temperature and actual temperature in the sample. Assuming that the influence of exothermic wax crystallization is negligibly small at a cooling rate of 0.2 °C/min, this conversion was also applied to wax containing samples.

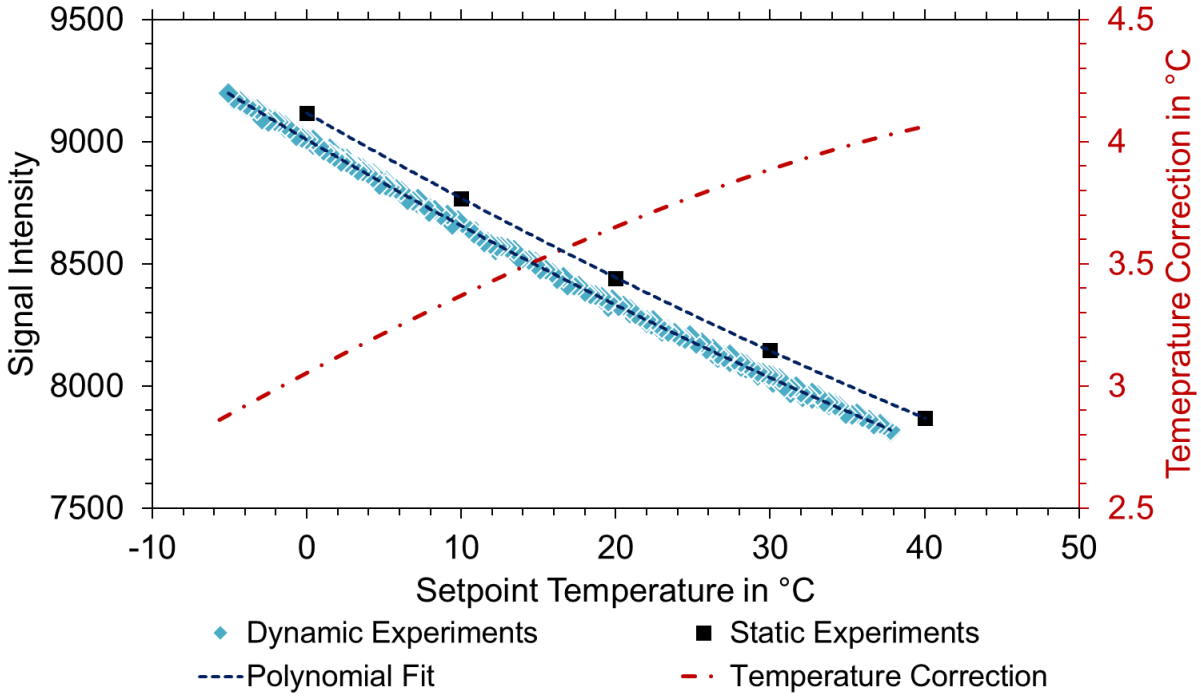

Fig. 3. Dynamic and static experiments for temperature calibration of NMR data with 5 wt% hexadecane in deuterated toluene.

Moreover, hexadecane did not precipitate over the entire temperature range tested. Experiments in Fig. 3 were therefore used to correct for the signal change with temperature due to the Boltzmann factor [57], which accounts for repartition of hydrogen atoms between the different energy levels. To do so, the signal intensity of solubilized wax S_{wax} was divided by the polynomial fit of dynamic experiments with 5 wt% hexadecane in deuterated toluene $\bar{S}_{hexadecane}$, yielding the corrected signal intensity $S_{corr,i}$ as shown in equation (2). The corrected signal was constant for temperatures above WAT, but unequal to 1 due to the difference in atomic ratio of hydrogen atoms of hexadecane and wax. As stated in equation (3), the corrected signal intensity was therefore normalized by dividing through the average signal intensity $\bar{S}_{corr}$ between setpoint temperatures 28 – 38 °C. This provided a measure for the total fraction of dissolved wax c_{liquid}, which is equal to 1 above WAT. From mass balancing, the apparent solid wax c_{solid} is implicitly given by equation (4). Due to the normalization procedure, additives were treated as part of the wax. This simplification is in analogy to DSC experiments, where the WPC is also measured in respect to the sum of precipitating components.

$$S_{corr,i} = \frac{S_{wax,i}}{\bar{S}_{hexadecane}(T_i)} \tag{2}$$

$$c_{liquid} = \frac{S_{corr,i}}{\bar{S}_{corr}} \tag{3}$$

$$c_{solid} = 1 - c_{liquid} \tag{4}$$

2.7. Filtration experiments and GC/MS

Changes in liquid phase composition were investigated after inducing wax crystallization through cooling and subsequent liquid phase recovery by filtration. Experiments were conducted with a 250 ml jacketed glass vessel, which was temperature controlled using a Julabo external Pt 100 sensor coupled

to a Julabo F-32 HE water bath filled with a 20/80 (vol/vol) mixture of ethyleneglycol in water. The sensor was directly immersed into the bulk sample, which was continuously stirred with a magnetic stirrer. A schematic of the setup is shown in Fig. 4. In experimentation, 150 ml of waxy solvent were filled into the vessel, both heated at 40 - 60 °C. The sample was allowed to equilibrate at 35 °C, after which cooling at a rate of 0.2 °C/min was applied. Sampling took place by piercing the PTFE/silicon septum at the bottom of the vessel with a needle and withdrawing 2 ml of sample, which was then filtered through a 0.45 µm PTFE filter membrane. Syringe needles, syringes, and filters were preconditioned isothermally at the target sampling temperature before sample withdrawal. The filtered sample was weighed and subsequently diluted with 85 g/g *n*-heptane, which also contained 4 mg/l heptadecane as internal standard for GC/MS analysis.

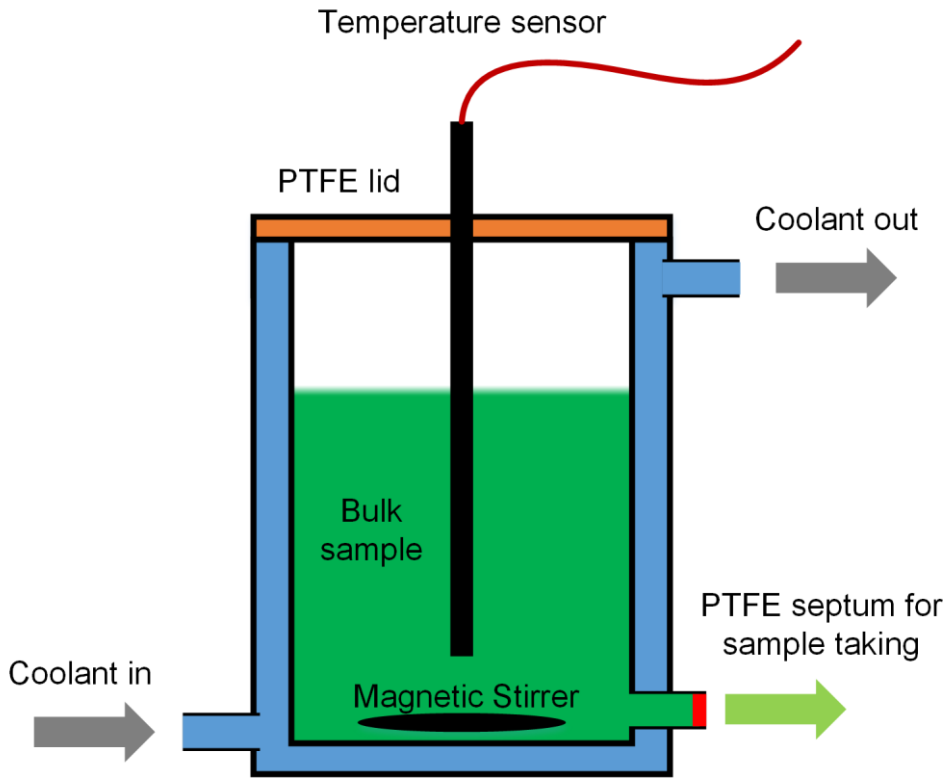

Fig. 4. Schematic of wax crystallization vessel

GC/MS analysis was performed on an Agilent 7890B with split/splitless inlet and a 7693A injection tower. A DB-1HT capillary column with 30 m length, 0.25 mm diameter, and 0.1 µm film thickness was used for separation. The GC was coupled to a 5977B mass spectrometer detector (MSD), which was set at 150 °C quad, 230 °C source, and 330 °C transfer line temperature. The MSD was set to a scanning range of 10 to 620 g/mol at a frequency of 4.6 scans per second, a step size of 0.1 m/z, and 6.5 min solvent delay. The inlet temperature was set at 330 °C. To quantify alkanes with a carbon number of $\leq C_{35}$, the inlet was operated in split mode at a split ratio of 1:20 and 2 µl sample injection. To measure alkanes with a carbon number of $\geq C_{30}$, the inlet was operated in splitless mode with 0.5 µl sample injection. Both modes had identical settings for oven program and flow of helium carrier gas. The oven temperature started at 50 °C, was first ramped to 90 °C at 20 °C/min, then to 180 °C at 10 °C/min, and lastly at 4 °C/min to 340 °C, where the temperature was held for 2 min. The flow of helium carrier gas was set to 1.2 ml/min with a holding period of 30 min, then ramped to 1.6 ml/min at a rate of 0.02 ml/min per minute and subsequently held constant.

Integration of elution peaks was done via MassHunter on the total ion chromatogram (TIC), excluding characteristic m/z values for molecules typically found in air. For quantification, the integrated peaks

were divided by the peak are of heptadecane internal standard. The detector response was nonlinear for all *n*-alkanes. Measurements were therefore done as interpolation from a calibration function, which had been fitted by nonlinear regression to four (split injection) or five (splitless injection) known dilutions of wax plus alkane standard mixture. This way, both the ratio of regarded *n*-alkanes in wax was determined, as well as a calibration function. Involved terms are shown in equations (5), (6), and (7), where a, b, c, a^*, b^*, and c^* are calibration constants, f_x is the ratio of a specific *n*-alkane in the wax, $\mathrm{C_x}$ is the *n*-alkane concentration (analyte) with according peak area $\mathrm{A_x}$, and C_{IS} is the internal standard (heptadecane) concentration with peak area $\mathrm{A_{IS}}$.

$$y(x) = \left(a\sqrt{x} + bx + cx^2\right)f_x = a^*\sqrt{x} + b^*x + c^*x^2, \text{ where} \tag{5}$$

$$y(x) = \frac{\mathrm{C_x}}{C_{IS}} = f_x \frac{\mathrm{C_{wax}}}{C_{IS}} \tag{6}$$

$$x = \frac{\mathrm{A_x}}{\mathrm{A_{IS}}} \tag{7}$$

As the standard mixture contained only even numbered *n*-alkanes, the response of uneven carbon numbers was obtained via polynomial interpolation. Two fittings are exemplarily shown in Fig. 5. The advantage of this procedure is that comparably few injections are needed for calibrating with sufficient resolution over a broad concentration range. This was deemed necessary, as the MSD response for *n*-alkanes showed variation during long injection series. The order of injections was also optimized to compensate for this drift. At first, a calibration series was run, then followed by sample injections pertaining to one wax crystallization experiment. Right after that, these injections were repeated in reversed order, followed directly by a second calibration run. Calibration was hence performed as average over two calibration series, which were run before and after each measurement series. Wax crystallization experiments were conducted in doubles, providing four measurement points in total per component.

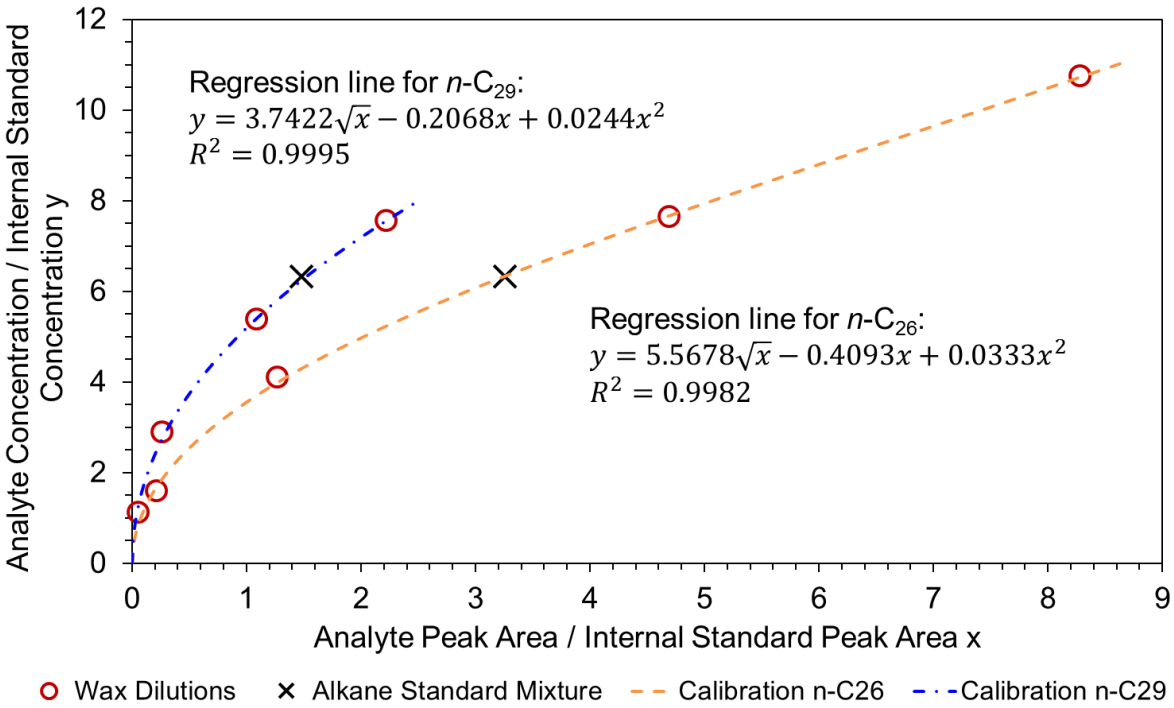

Fig. 5. Exemplary regression lines for calibration of *n*-C26 and *n*-C29 for GC/MS analysis.

3. Results and discussion

To provide a complete picture, PPD precipitation and effect on wax crystallization is first discussed as studied by established techniques such as DSC, rheometry, and CPM. Secondly, the main advancement of this study is presented and discussed, which comprises PPD-wax interactions in liquid phase studied by NMR and GC/MS, and additionally a WPC method comparison. Sample concentrations of 1000 ppm PPD and 5 wt% wax in toluene were used consistently throughout all experiments. The concentration of PPD is thereby higher than usual in petroleum production, which was deemed necessary to obtain well-quantifiable differences between the additives.

3.1. PPD characterization and effect on wax crystallization

3.1.1. PPD precipitation in pure solvent studied by DSC

The precipitation behavior of different PPD chemistries was first observed in DSC, using 5 wt% PPD in toluene without the addition of wax. As shown in Fig. 6, each PPD has one or two characteristic precipitation peaks. The precipitation onset temperature was determined with the same procedure as the WAT. For all PPDs, the precipitation onset was detected before the main peak. The peak shape of PPD B is narrower than that of PPD A, which suggests a lower degree of polydispersity. Also, PPD A and PPD B show one main peak between 0 and -10 °C, and a smaller peak between -25 and -40 °C. This secondary peak could be explained by unreacted monomer or remaining solvent in the sample. The crystallization temperature as well as total heat released by PPD C is lower than for PPD A and PPD B, indicating a lower tendency to crystallize in toluene solvent. Experiments in Fig. 6 show data with a cooling rate of 5 °C/min, because this provides a better illustration of the polymer precipitation profile. PPDs were also measured at a cooling rate of 0.2 °C/min and the characteristic peaks followed the same trends.

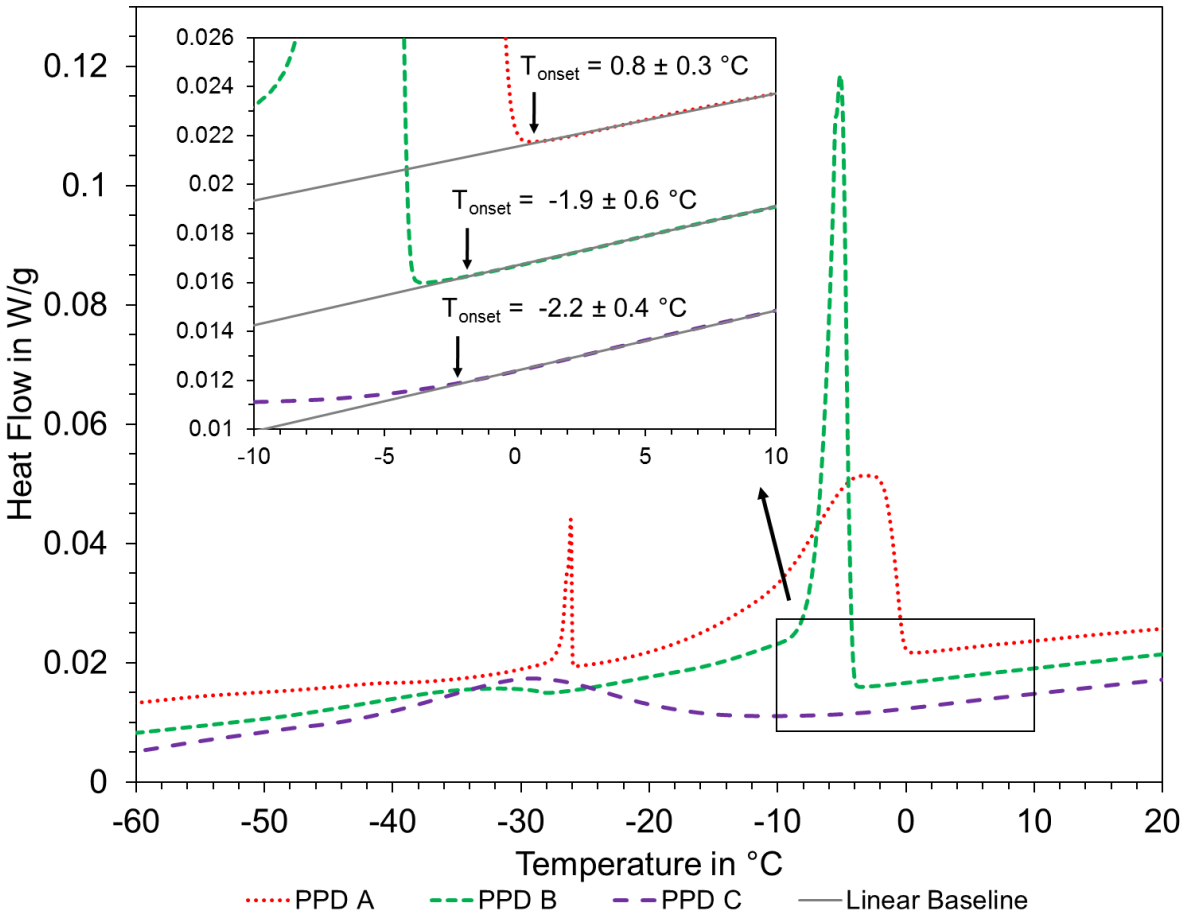

Fig. 6. DSC heat flow of 5 wt% PPD in toluene at a cooling rate of 5 °C/min. Graphs were shifted on the y-axis for better overview.

3.1.2. Influence of PPD on wax precipitation studied by DSC

To ensure comparability with other experiments, DSC employed a cooling rate of 0.2 °C/min. This cooling rate is low compared to the usual operating settings for DSC. To improve the signal to noise ratio, at least four repetitions of identical measurements were run and the final graph was averaged over these. Fig. 7 shows the noise improved results for DSC measurements of different additives with 5 wt% wax in toluene. Data was reproducible within a certain margin of error, as indicated by the standard deviation. According WAT values are listed in Table 2, which were computed as the heat flow exceeding the linear baseline prior to wax precipitation. Addition of PPD A amounted to the largest decrease in WAT, which can also be seen in Fig. 7 as shift in the main peak to lower temperatures. For all samples, a strong increase in heat flow was observed between 18 – 20 °C, marking the onset of the main peak. For all samples except PPD A, the WAT was measured 1 – 4 °C higher than the onset of this main peak. The WAT is visible as slightly scattered, but distinct change in slope of the heat flow. WAT determination via exceeding the linear baseline was chosen over the tangent intersection procedure, as this provides a more sensitive estimate of the WAT [51]. It has to be noted, that scattering of up to 1 °C in WAT is common for this type of measurement and sample. This extent of data scattering is well in line with the standard deviation presented in Fig. 7, however, the difference in WAT between PPD B, PPD C, and asphaltenes in Table 2 have to be interpreted with care. The peak shape for PPD C, asphaltenes, and no PPD is similar. Other authors also found asphaltenes to decrease WAT with little impact on the shape of the wax crystallization peak [21]. For PPD A and PPD B it appears that two additional peaks are superimposed onto the main crystallization peak. In particular, PPD B shows such

an imposed peak between the temperatures 0 – 5 °C. These peaks are likely to be the result of the bimodal crystallization peaks shown in Fig. 6 for PPDs in pure solvent. However, the intensity change per mass of polymer is higher than for pure PPD solutions of Fig. 6, which would suggest co-crystallization of wax at these temperatures, also.

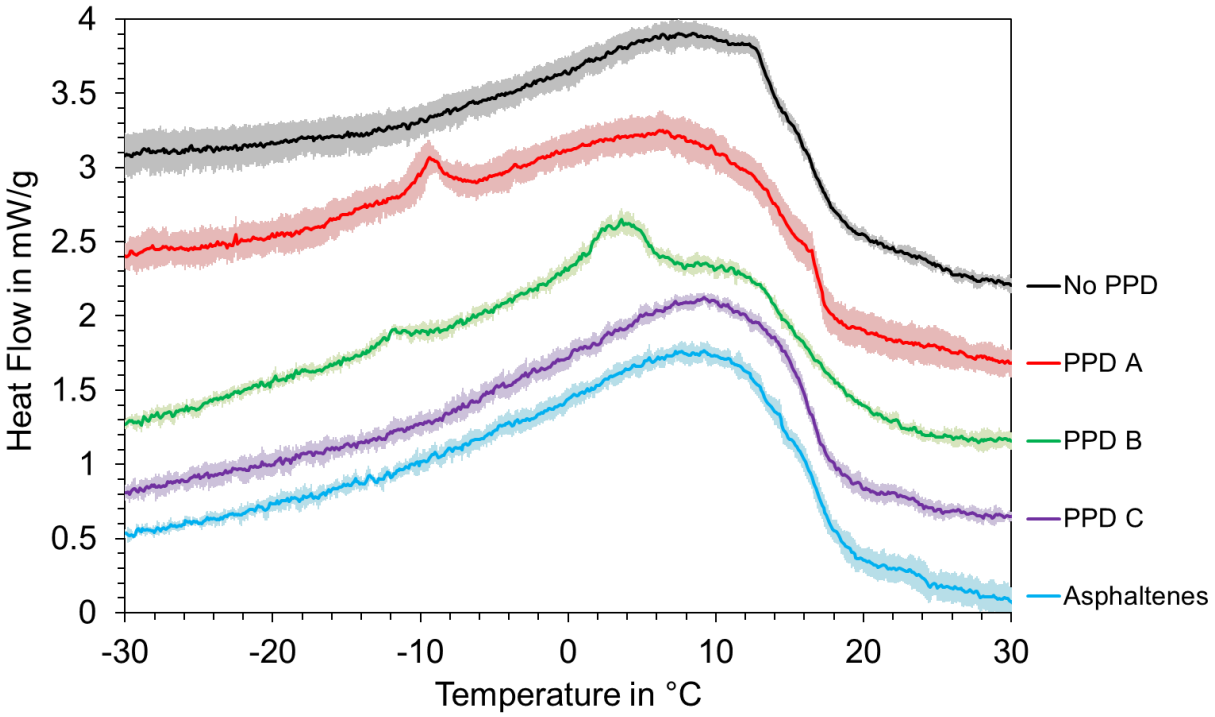

Fig. 7. DSC heat flow for 1000 ppm PPD or asphaltenes and 5 wt% wax in toluene. Each graph represents the average over at least four identical measurements to improve signal to noise ratio, where the shaded area marks the standard deviation. Graphs were shifted on the y-axis for better overview.

Table 2. Computed WAT from DSC data.

Sample	WAT in °C
5 wt% wax in toluene	25.2
1000ppm PPD A and 5 wt% wax in toluene	18.5
1000ppm PPD B and 5 wt% wax in toluene	22.5
1000ppm PPD C and 5 wt% wax in toluene	23.7
1000ppm asphaltenes and 5 wt% wax in toluene	23.9

3.1.3. Influence of PPD on wax crystallization studied by rheometry and CPM

The efficiency of PPDs and asphaltenes for improving flow-ability of the waxy model oil was tested by rheometry and CPM. Viscometry measurements in Fig. 8 show three distinctive regions of precipitation. At temperatures above Region 1, no wax crystallization was observed by viscometry, which is in part due to the low shear rate imposed. Region 1 then marks the crystallization onset, where an increase in apparent viscosity by several orders of magnitude was recorded for all additives except for PPD A. In region 2 the apparent viscosity further increases due to continued wax crystal growth. In region 3 the crystal growth continues, but gel degradation effects due to continuous shearing lead to an apparent viscosity decrease for all additives except in presence of PPD A. For no PPD and PPD A, the apparent viscosity increased continuously as cooling progressed. It has to be noted that for all samples except for PPD A, the minimum torque required for reliable measurement was reached 1 – 4 °C below the WAT listed in Table 2.

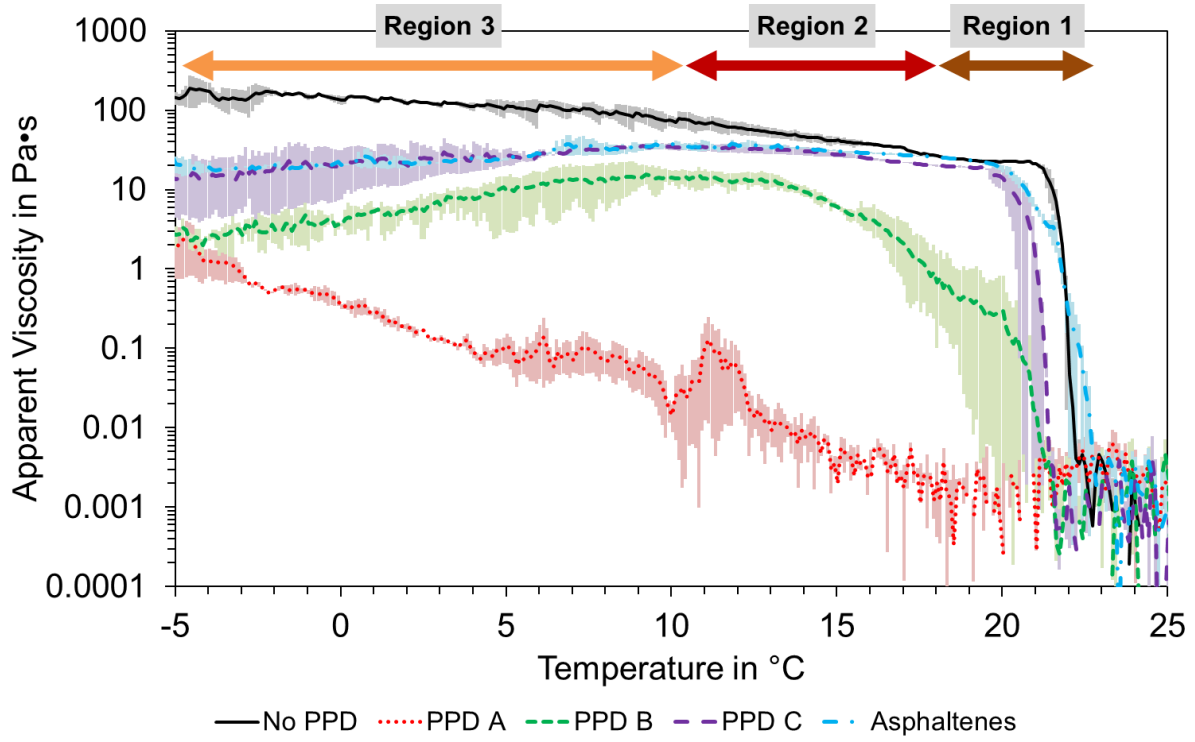

Fig. 8. Viscometry results for 1000ppm PPD and 5 wt% macrocrystalline wax in toluene at a shear rate of 0.1 s^{-1}. A cooling rate of 0.2 °C/min was applied and the graphs represent the average of two to three measurements. Error bars mark minimum and maximum values. Three different regions can be distinguished: Region 1 (Wax crystallization onset), Region 2 (wax crystal growth), and Region 3 (continued crystal growth and gel degradation).

The effect of PPD or asphaltene addition on wax crystallization under quiescent conditions is illustrated in Fig. 9. The observation temperature was chosen at -2 °C to reveal wax crystal morphologies at the lower end temperature of subsequent NMR and GC/MS experiments. The additive free case showed wax crystallization with co-joined structures in the size range of 50 µm and more. Clustering of multiple layers around a stearic center can be observed, and the individual branches are mostly straight. Such structures can be interpreted as needle-shaped crystals that are cross-linked to form 3D structures. Alternatively, the observed geometries could represent plate shaped crystals that are skewed with respect to the plane of observation. Addition of PPD A and PPD B both resulted in the formation of distorted and smaller crystals with the lowest yield strength. PPD A led to the formation of small and finely dispersed wax crystals. PPD B addition resulted in roundly shaped crystal clusters. Both PPD C and asphaltenes also showed the formation of more finely dispersed wax crystals. In case of PPD C, the CPM image appears to contradict yield strength measurements, since crystal dimensions were shown to be smaller than without additive. However, the crystal network appeared denser, which could explain that the resulting yield strength was higher. Asphaltene addition significantly lowered gel yield strength and the crystal network is also less dense than for PPD C.

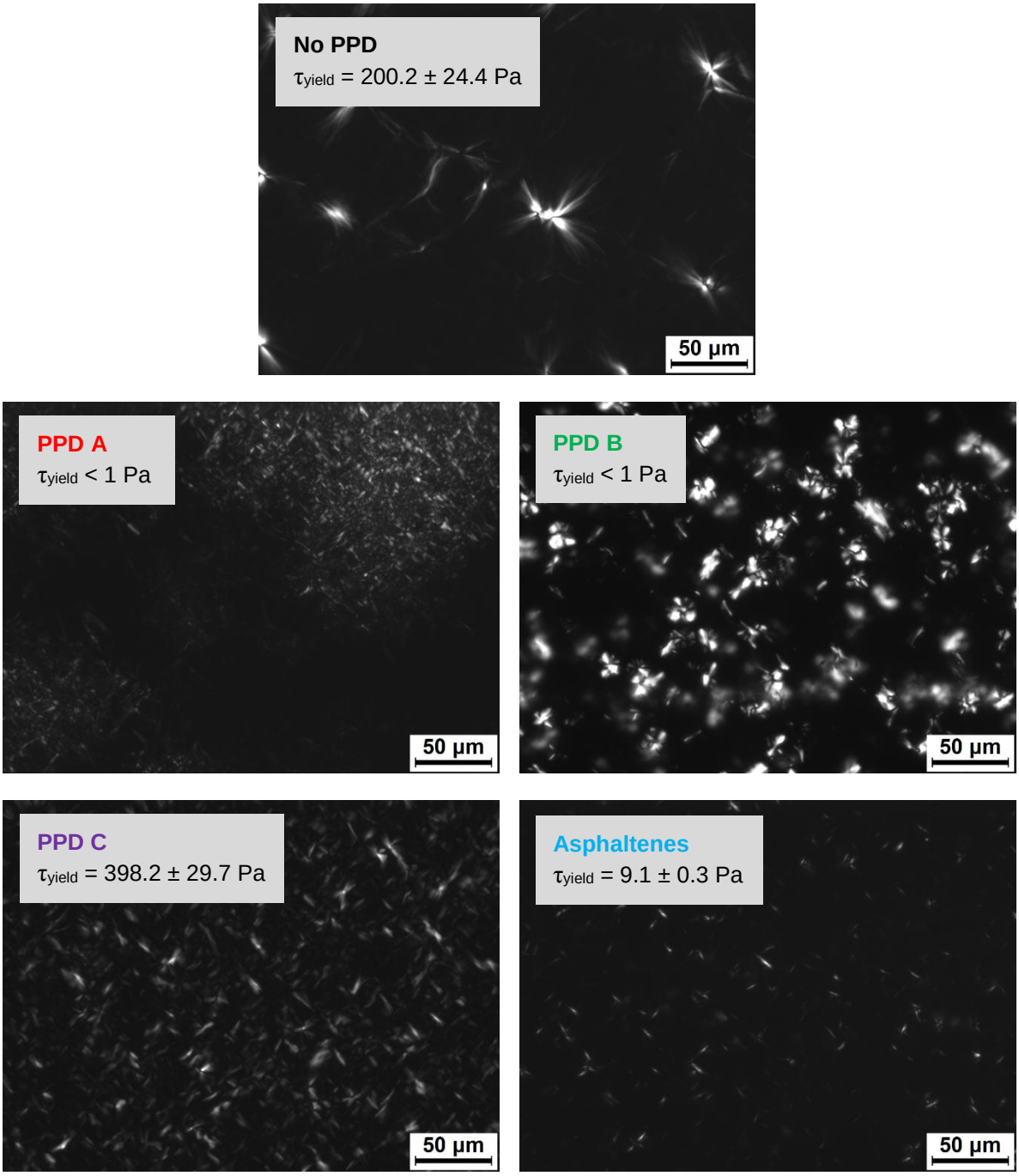

Fig. 9. CPM images of 1000 ppm PPD and 5 wt% macrocrystalline wax in toluene at -2 °C. The according gel yield strength as averaged over two to four rheometry experiments is shown as well.

Comparing the results of viscometry and gel yield strength, there appears to be a difference in additive effect depending on the shear conditions during wax crystallization. It has been pointed out by other authors that increased shearing can result in the reduction of gel yield strength due to the rupture of crystal-crystal linkages [13, 58]. As a result, at -2 °C both asphaltenes and no PPD show shear stresses that are approximately two orders of magnitude lower after continuous shearing than the yield stresses after quiescent cooling. Also, a significant improvement of flow-ability was made by addition of PPD C as shown in Fig. 8, whereas in Fig. 9 the gel yield strength was higher compared to the additive free case. Shearing therefore can improve the effect certain PPDs have on waxy gelation. All in all, the results are in agreement with other studies published on the effect of PPD or asphaltene on wax crystallization and gelling [30, 35, 47, 59-62]. Moreover, it can be concluded that PPD A and PPD B

are efficient wax inhibitors for the waxy model oil. Asphaltenes also showed beneficial influence on wax crystallization, but PPD C exhibited poor wax inhibition efficiency for the tested system.

3.2. Inhibitor-wax interactions studied in liquid phase by NMR

The T_2-distributions from NMR measurements are displayed in Fig. 10 for qualitative comparison. Each sample produced a characteristic and reproducible distribution. The data is presented in raw form without correction for the temperature lag in the sample. Experiments with a monodisperse, non-crystallizing alkane (hexadecane) in deuterated toluene resulted in a single peak. This peak shifted towards shorter T_2 with decreasing temperature due to increasing viscosity, hence a reduction in diffusion coefficient and therefore C_{16} mobility. Artifacts at T_2 of 10^{-3} s and shorter appear in all distributions, but are more pronounced when additives were added and after solid wax had formed.

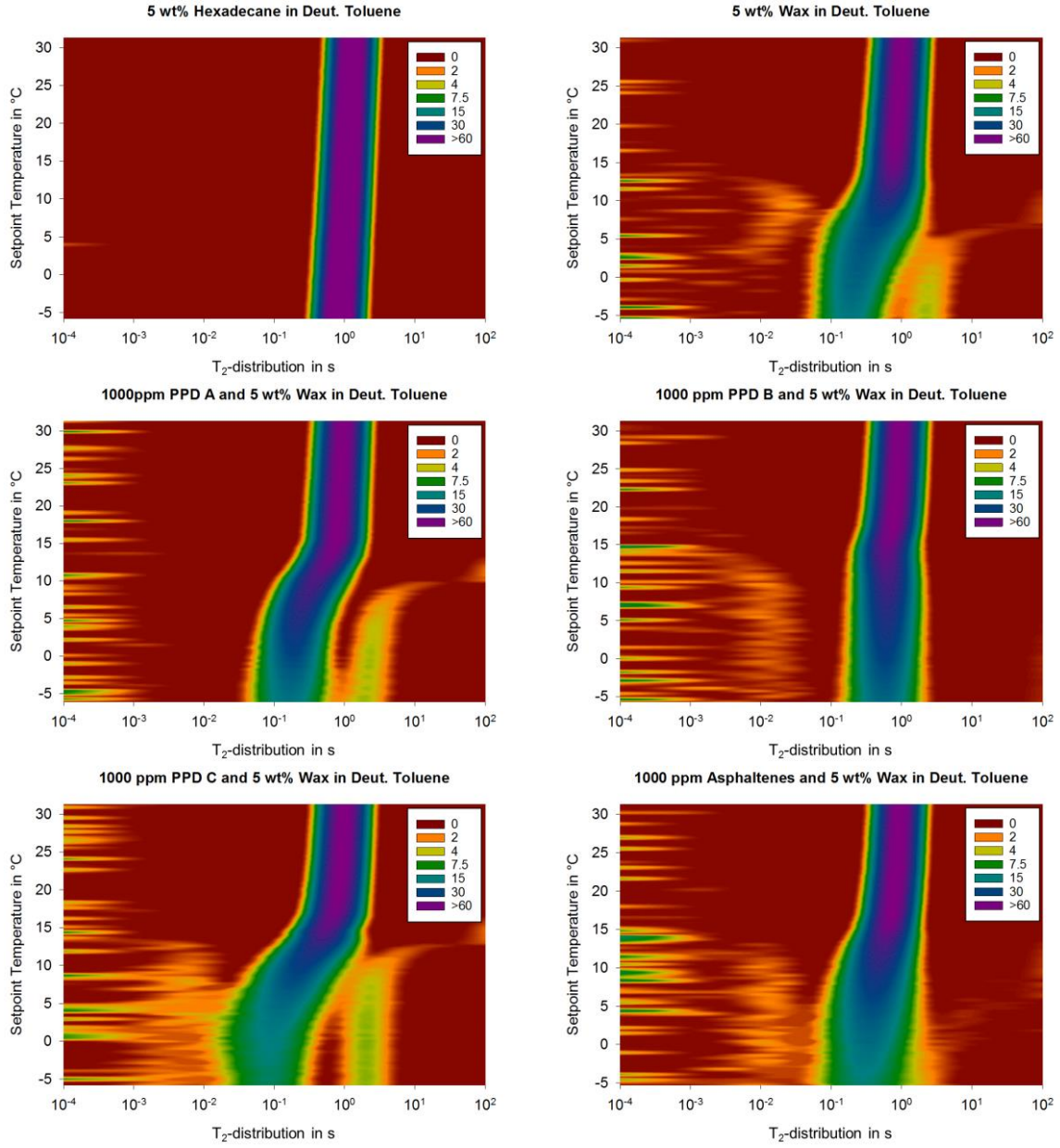

Fig. 10. NMR T_2-distribution in dependence of (uncorrected) setpoint temperature. Each measurement was made on 3 g solution of 5 wt% alkanes in deuterated toluene with and without 1000 ppm PPD.

Analogous to the hexadecane sample, the main peak in the T_2-distribution of 5 wt% wax in deuterated toluene shows a shift to lower T_2 with decreasing temperature. Below 15 °C setpoint temperature, wax

crystallization is visible as broadening of the main peak and signal intensity decrease. This intensity decrease is due to the precipitation of dissolved wax molecules, which invokes T_2 decreases below 10^{-3} s^{-1} for the affected molecules. In other words, the phase change is reflected by affecting the mobility of wax. Moreover, two secondary peaks can be observed. One secondary peak is at T_2 of 10^{-2} s and above, the other one appears at $10^0 – 10^1$ s.

Secondary peaks at shorter T_2 are the results of spatial hindrances imposed on the bulk fluid by particles in the dispersion [63]. The growing wax crystals therefore act to partially decrease liquid wax mobility. Such a decrease is the result of liquid wax molecules that are 'bond' by the proximity to solid wax crystals [64]. Interestingly, PPD A showed a suppression of the regarded peak. PPD C and asphaltenes resulted in an enhancement of the secondary peak at low T_2. Additives therefore appear to influence interactions at the solid-liquid interface and can possibly suppress intermediate states.

The secondary peak at long T_2 ($10^0 – 10^1$ s^{-1}) appears counterintuitive at first, but has been detected for the additive free sample, PPD A, and PPD C. An increase in liquid wax mobility is inconsistent with the idea of an imposing solid crystal structure. Moreover, no physical meaning can be attributed with T_2 larger than 10^1 s^{-1}. The most likely explanation is that the inverse Laplace routine is splitting a single peak into two, as this routine is mathematically ill posed. Depending on the smoothing factor, the secondary peak with the longest T_2 was observed to change position and intensity. The secondary peak occurring at T_2 of approximately 10^{-2}, however, was less or not at all affected by the smoothing factor, which indicates significands of this peak.

All in all, efficient additives (PPD A and PPD B) resulted in more defined states, whereas PPD C with poor inhibition performance led to a broadening of the T_2 distribution, which could indicate a blurring of the solid-liquid transition. A previous study reported similar results, i.e. a shift towards shorter T_2 with lower signal intensity during wax crystallization in deuterated solvent [46]. PPD additives were also found to delay wax crystallization and reduce the amount of apparent solid wax, but the occurrence of secondary peaks in T_2-distribution had not yet been considered.

3.3. Wax precipitation studied by GC/MS

Based on the results of previously discussed experiments, liquid phase sampling was conducted at 18 °C down to -2 °C in 4 °C intervals. The induced shear of the magnetic stirrer (850 RPM) was sufficiently large, so that the wax dispersion remained free flowing. Gelling could be observed close to surface level, but never in the bottom two thirds of the sample bulk. CPM was used to screen the filtration procedure at a sampling temperature of 6 °C. None of the tested samples showed solids remaining in the filtrate.

Fig. 11 shows the absolute concentration of *n*-alkanes from C_{22} to C_{40} of the additive free sample. As the temperature is cooled down, the liquid phase contains less *n*-alkanes. Data was reproducible within a certain margin of error. With decreasing sampling temperature, the carbon number of affected *n*-alkanes shifted from higher to lower molecular weight. The study of compositional change was limited to *n*-alkanes with carbon numbers of C_{20} to C_{40} for several reasons. Firstly, the largest change in concentration was observed for *n*-alkanes in the range of C_{22} to C_{40}. Secondly, *n*-alkanes with a higher molecular weight than C_{40} were excluded, as accurate quantification was made difficult by a low response of the MSD detector for high boiling point substances. Thirdly, quantification of *iso*-alkanes was not accurate enough. This was due to low intensity peaks with broad spanning elution times. Moreover, the detector response could not be calibrated for *iso*-alkanes, due to a lack of structural information and hence an appropriate calibration standard.

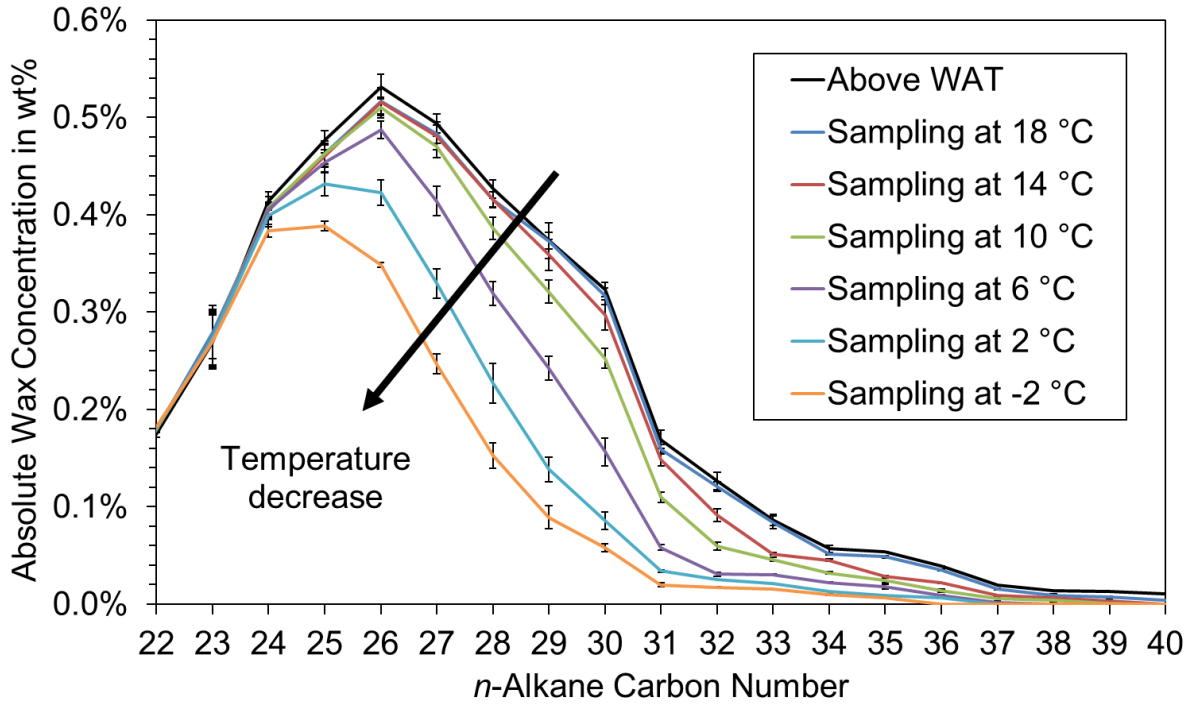

Fig. 11. Composition of *n*-alkanes between C_{22} and C_{40} for 5 wt% wax in toluene at different temperatures of sample taking. Error bars represent the standard deviation from the average of four measurements.

To compare the influence of different additives on wax crystallization, the change in composition was considered rather than absolute concentrations. An advantage is that this approach provides a more sensitive estimate of affected molecular weight regimes. A disadvantage is that subtracting two similar values amplifies the relative error. As a result, the compositional changes illustrated in Fig. 12 should be interpreted in terms of general trends, i.e. multiple component trends rather than individual concentration changes. Still, as can be seen in Fig. 11 the standard deviation of individual concentrations is significant for the majority of measurements. In particular, at sampling temperatures between 14 °C and -2 °C, almost all changes in concentration differ by a multiple of the respective standard deviation. The depicted trends are therefore statistically significant. The wax concentration decrease in Fig. 12 was calculated as difference of two subsequent measurements, i.e. the decrease at 14 °C yields the composition 18 °C minus the composition at 14 °C and so forth. All systems show similar trends, which followed three distinct steps:

Step (i) Right after wax crystallization onset, *n*-alkanes are depleted on a broad range of molecular weights (above WAT to 18 °C).

Step (ii) As wax precipitation continues, the affected range of wax molecular weight is shifted to a narrower region of *n*-alkanes, which bears similarities to a Gaussian bell curve (18 °C to 10 °C).

Step (iii) As sampling temperatures decreases even further, the bell-shaped curve is shifted to affect lower molecular weight *n*-alkanes (10 °C and below). This is due to depletion of higher molecular weight alkanes and due to temperature induced precipitation of lower molecular weight alkanes.

The results are in agreement with the view that lower temperatures can induce wax crystallization of lower molecular weight alkanes, also. The addition of PPD A shows lower and narrower *n*-alkane decreases during step (i) and (ii). PPD B addition delayed step (i) down to 14 °C, which was observed for other samples until 18 °C only. The overall sum of component loss during step (i) appears to be the lowest for asphaltenes. However, higher molecular weight components are depleted to a larger extent between 14 °C and 2 °C than this is the case for other samples. This indicates that asphaltenes do not

necessarily delay wax precipitation, but favor the depletion of low molecular weight components first. A similar observation was made by Chen et al. after addition of poly alkyl methcrylate or alkyl naphthalene copolymer [65]. In contrast to that, PPD A displays prolonged depletion of high molecular weight components. This can be seen e.g. in a lower decrease of C_{36} to C_{38} at 18 – 14 °C, but an above average decrease of these components at 10 °C and lower. For PPD A and PPD B, the general shape of the concentration decrease appears narrower at sampling temperatures of 6 °C and 2 °C than for PPD C.

In a previous study, Paso et al. published similar results on *n*-alkane depletion during wax crystallization [47]. Temperature decrease was also found to lead to the depletion of higher molecular weight alkanes during later stages of wax crystallization. However, depletion *n*-alkanes on a broad range of molecular weight (step (i)) was found to stretch over a larger temperature regime (up to 30 °C) than as the results in Fig. 12. Moreover, the current study showed *n*-alkane depletion to take place more progressively, i.e. less rapid changes in total wax content with decreasing temperature. Still, such phenomena are governed by the initial wax composition. The Fischer-Tropsch waxes used by Paso et al. had lower molecular weight and lower isomer content than the wax used in this study [47]. Also, the previous study featured equilibrated systems, whereas a constant cooling rate was applied in this study. The results were therefore not found to be contradicting.

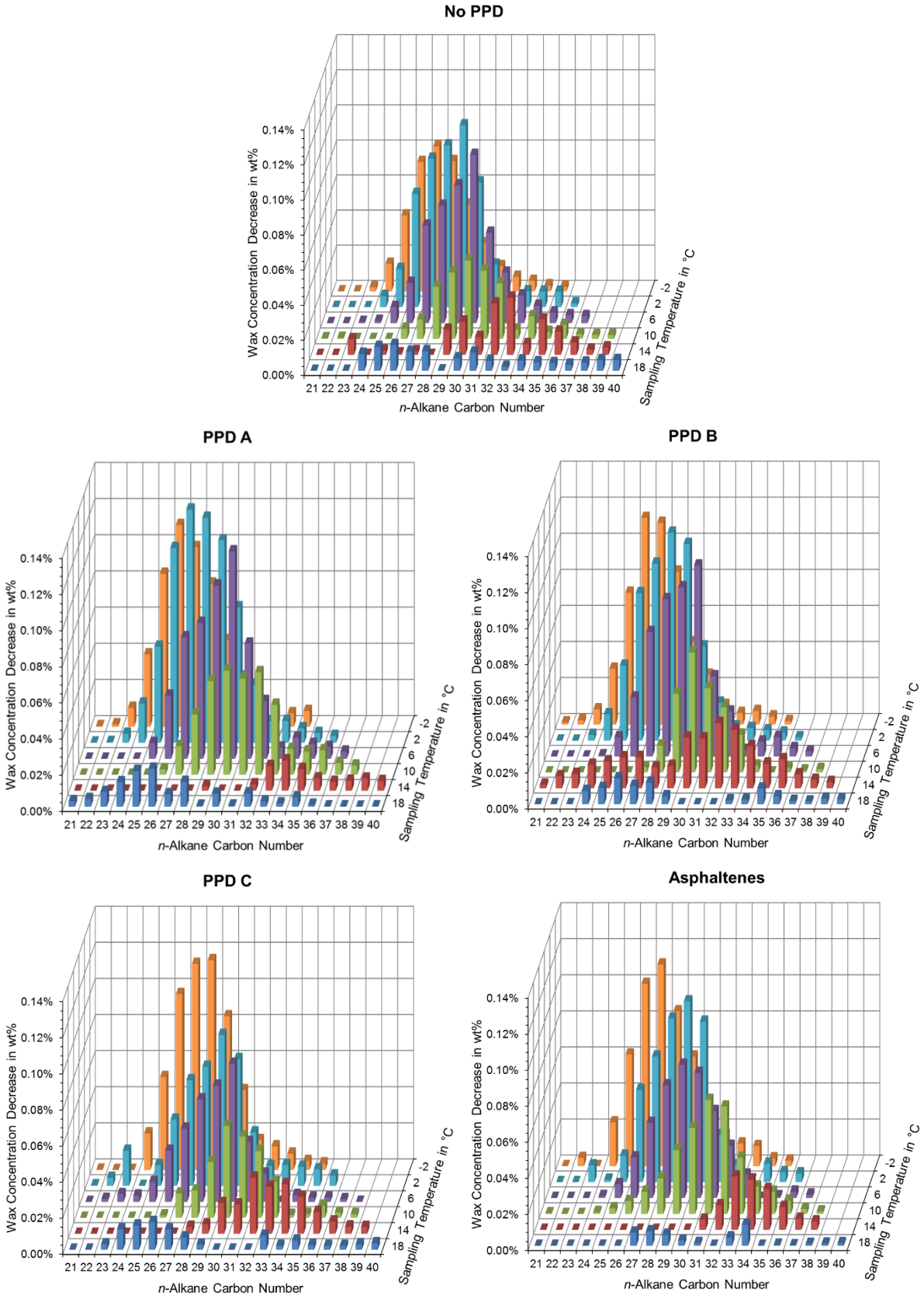

Fig. 12. Changes of *n*-alkane content in liquid phase as measured by GC/MS. Each sample consisted of 1000 ppm PPD or asphaltenes and 5 wt% wax in toluene. The wax concentration decrease was computed by subtracting each alkane concentration from the next higher temperature concentration.

3.4. PPD Effect on Wax Precipitation Curve (WPC)

The data of Fig. 7 was converted into the WPC via the procedure described in section 2.3 and results are displayed Fig. 13. All PPDs induced temperature depression of the WPC, but not asphaltenes. For PPD A, the WPC depression is similar to translating the WPC of additive free experiments by 2 – 3 °C. In other words, the curves are almost parallel on the temperature interval between 15 °C and -5 °C. For PPD B there is approximately no reduction in precipitated wax until 15 °C. After that the WPC depression surpassed even PPD A. PPD C yielded notable reduction in precipitated wax only below 10 °C. The trends for WPD depression correspond with the order of polymer precipitation of Fig. 6, i.e. PPDs with a higher precipitation onset temperature also started to decrease the amount of precipitated wax in Fig. 13 at higher temperatures. Asphaltenes did not induce WPC depression that was statistically significant. The WPC curves of no PPD and asphaltenes are almost identical.

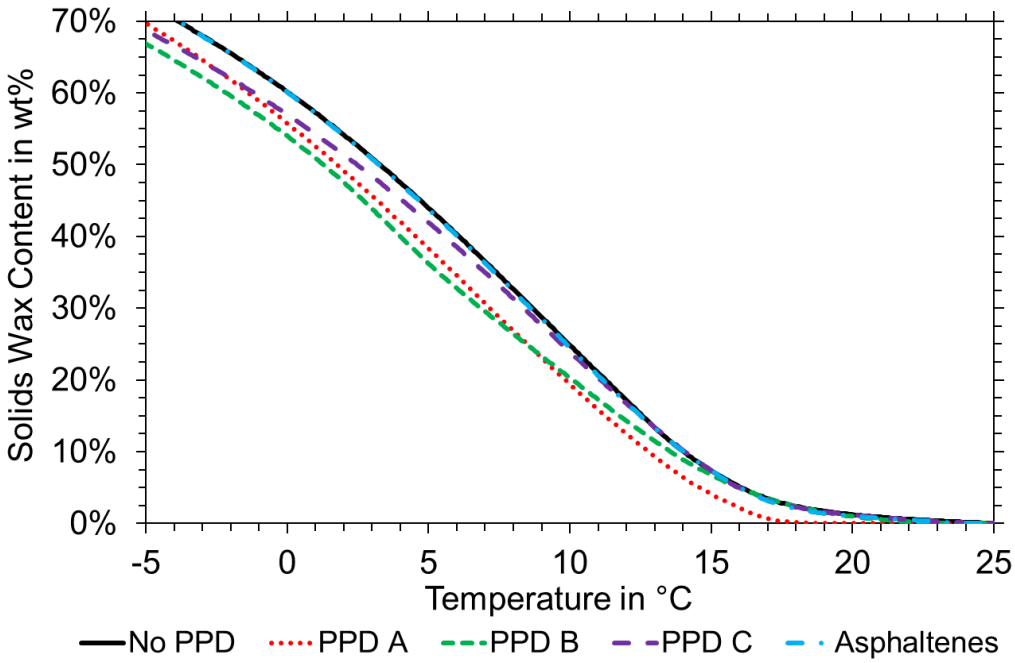

Fig. 13. Solid wax in percentage of total wax content from DSC measurements of 1000 ppm PPD or asphaltenes and 5 wt% wax in toluene. Lower temperatures were omitted from the plot for better overview.

The T_2-distributions in Fig. 10 were converted into WPCs via the in section 2.6 described procedure. As can be seen in Fig. 14, the apparent solid wax started increasing at approximately 25 °C for all samples except for the sample containing PPD A. As in DSC experiments, PPD A induced the largest crystallization lag. The WPC depression induced by PPD B starts to be statistically significant below 15 °C. On average, asphaltenes accounted for higher apparent solid wax than samples containing PPD A or PPD B. However, some differences can be notices for comparing WPC of NMR and DSC. In NMR, asphaltenes reduced the amount of precipitated wax in comparison to the additive free case, which was not the case in DSC. The presence of PPD C even increased the apparent solid wax in NMR. The amount of data scattering is largest for PPD C, which is due to the blurring of solid and liquid phase contributions in the T_2-distribution at around 10^{-3} s.

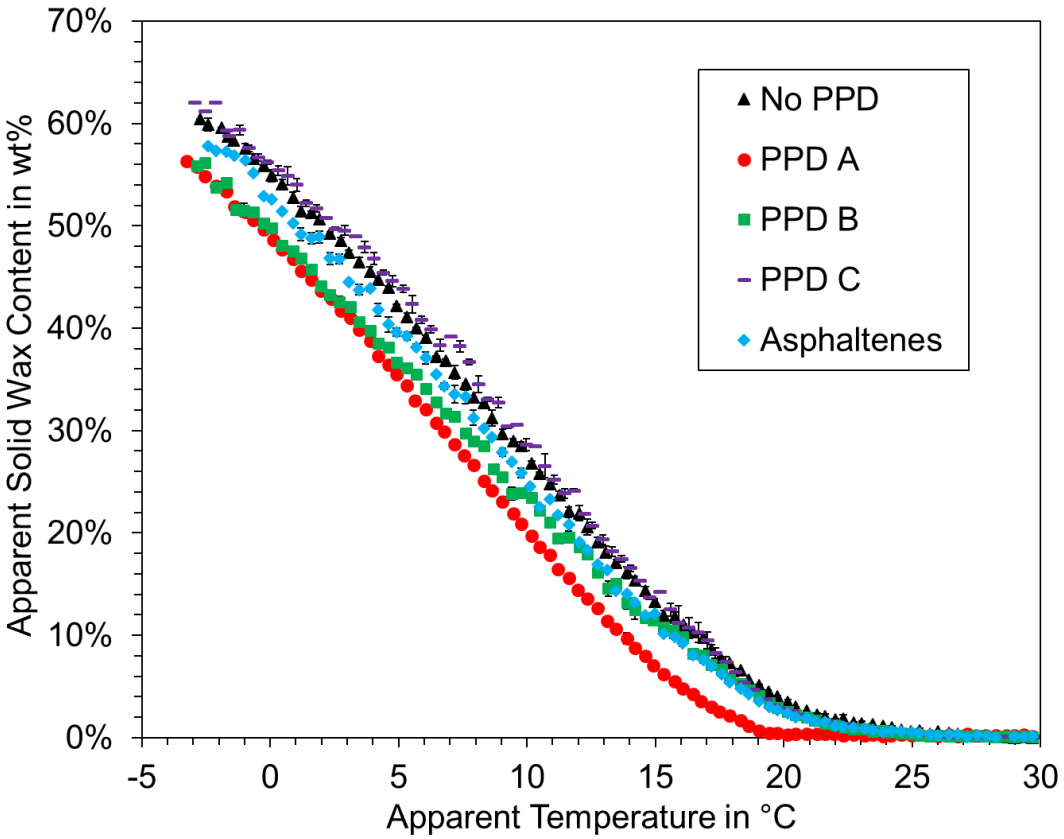

Fig. 14. Apparent solid wax in percentage of total wax content from NMR measurements of 5 wt% wax in deuterated toluene with and without 1000 ppm PPD or asphaltenes. Graphs represent the average of two identical measurements with maximum and minimum as error bars.

To approximate the WPC by given data from GC analysis, the relative decrease $p_{\%}$ in C_{20} to C_{40} *n*-alkane was computed. Following equation (8), this decrease was calculated as the sum of *n*-alkanes at a certain sampling temperature $c_i(T_{sample})$ divided by the sum of all measured *n*-alkanes $c_i(T_{above\,WAT})$. This percentage is only an approximation of the actual WPC, especially as not all precipitating components are included.

$$p_{\%}(T_{sample}) = 100\% - \frac{\sum_{i=20}^{40} c_i(T_{sample})}{\sum_{i=20}^{40} c_i(T_{above\,WAT})} \tag{8}$$

As can be seen in Fig. 15, the *n*-alkane decrease increases for all samples as the sampling temperature is lowered. The relative error was computed according to the propagation of uncertainty, but is not visible in Fig. 15 due to low values. The depicted differences therefore carry a high statistical significance. For PPD C and asphaltenes, the *n*-alkane decrease is lower than the additive free sample at temperatures of 2 – 14 °C. For PPD A and PPD B, the relative decrease is higher than the additive free case at 6 °C and below. These results are counter intuitive due to a reversed trend as compared to WPCs obtained by DSC (Fig. 13) and NMR (Fig. 14). Since two other techniques show a lower total amount of precipitated wax with PPD A and PPD B, it appears that these additives promote precipitation of C_{20} to C_{40} *n*-alkanes over other components. Such an observation makes sense from the viewpoint that industrial PPDs, especially comb polymers, are often tailored to chemically match the wax molecules responsible for gelling [6, 34]. A possible explanation is therefore that PPD A and PPD B increase selectivity for precipitation of *n*-alkanes over *iso*-alkanes, which were quantified in DSC and NMR, but not in GC/MS. However, more data is needed to confirm this influence on selective wax precipitation.

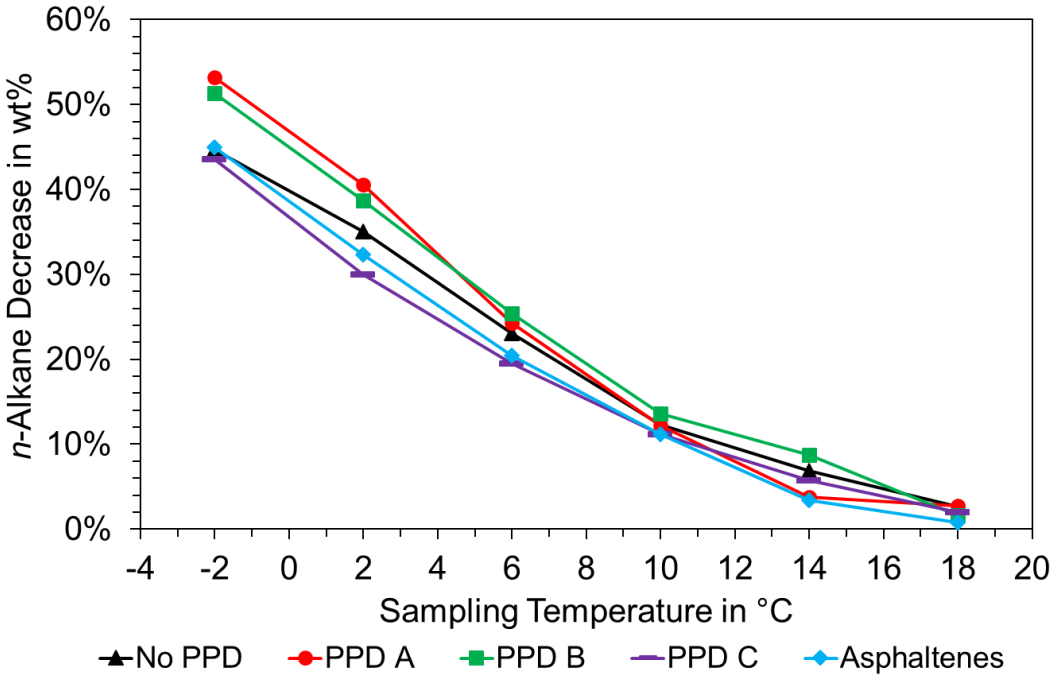

Fig. 15. Percentage of *n*-alkane decrease as measured by GC/MS.

To compare the different techniques employed for WPC determination, results of DSC, NMR, and GC/MS are plotted together in Fig. 16. No PPD and PPD A were selected to represent the base case and one additive with strong effect on wax precipitation. As can be seen, the techniques do not superimpose, but the depicted tendencies are the same. Regarding GC/MS results, the graphs are naturally different from DSC and NMR, as only 84.6 wt% of the total wax was considered. NMR technique shows an earlier onset of wax precipitation than DSC for both samples. In fact, the T_2 in NMR is decreased by several orders of magnitudes, whereas the relative change in DSC heat flow is comparatively low when wax crystallizes, which implies that NMR could be more sensitive. The fact that DSC measured a higher solid wax content than NMR below 8 °C could be due to the temperature correction function, as this does not account for exothermic wax crystallization. On the other hand, WPC computation in DSC involved a polynomial baseline fitting to calculate the excess heat. This baseline might not fully represent the involved physics, as heat capacity changes as a function of the total solids content. Moreover, the difference in molecular weight of deuterated and non-deuterated toluene could influence solubility of the wax. Interestingly, the temperature lag induced by PPD A remains almost constant for both NMR and DSC results, which in turn suggests good comparability of these techniques.

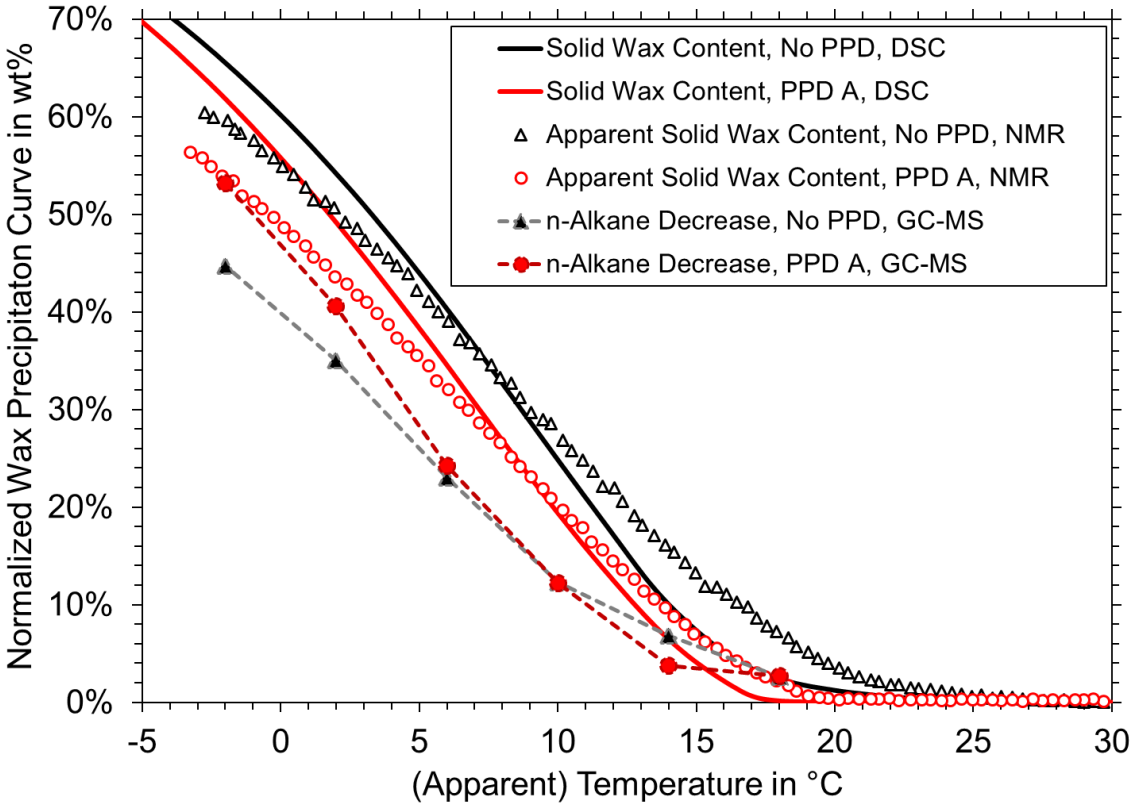

Fig. 16. Comparison of normalized WPC determined by different techniques for samples of 5 wt% wax in toluene with and without 1000 ppm PPD A.

4. Conclusion

In this article, the effect of chemical additives on wax crystallization was studied in a waxy model system using both established techniques and new approaches. Firstly, additive efficiency was characterized by the use of DSC, rheometry, and CPM. Secondly, PPD-wax interactions in liquid phase were mapped via new approaches in NMR and GC/MS. In addition, a comparison of WPC among different techniques was made. Main results and conclusions are summarized below.

1. The chemical additives showed different effect on apparent viscosity, gel yield strength, and crystal morphology as determined by rheometry and CPM. Efficient wax inhibition was attributed with PPD A and PPD B, leading to a change in wax crystal morphology towards smaller and more compact crystals with lower propensity to overlap, which further reduced apparent viscosity of the waxy dispersion, and gel yield strength. Asphaltenes induced similar, but less pronounced effects, and PPD C could both improve as well as aggravate waxy oil flow-ability.
2. The T_2-distribution of NMR experiments indicated the formation of intermediate states during solid-liquid transition, where dissolved wax molecules displayed increased as well as reduced mobility. Most likely, these intermediate states represent dissolved wax 'bond' by the proximity to solid wax crystals [64]. Efficient inhibitors (PPD A and PPD B) could suppress certain states, whereas PPD C led to a blurring of the solid-liquid transition in the NMR T_2 distribution.
3. Following wax crystallization experiments with liquid phase extraction, GC/MS component analysis revealed *n*-alkane depletion to happen in three distinct steps. Wax precipitation started with the reduction of *n*-alkanes on a broad range of molecular weight (step i). At lower temperatures, the concentration decrease would affect narrower *n*-alkane regions (step ii),

which would decrease in average molecular weight at even lower temperatures (step iii). Chemical additives could affect compositional changes during wax crystallization and efficient inhibitors were shown to delay step i and step ii.

4. Both DSC and NMR showed delayed crystallization onset and a reduction in the amount of precipitated wax for efficient additives (PPD A and PPD B). Combining these techniques with results from GC/MS suggested that additives with efficient wax inhibition may at the same time increase selectivity for *n*-alkane precipitation. All in all, the different approaches for WPC determination did not superimpose, but general trends were similar.

In conclusion, new procedures for studying PPD-wax interactions by the use of NMR and GC/MS technique were presented. Testing shows potential for these to investigate wax inhibition phenomena more closely. Moreover, the link to additive characteristics with importance to flow assurance was made. Comparison indicated that additives with efficient wax inhibition as determined by DSC, CPM, and rheometry also showed characteristic behavior in NMR and GC/MS, such as the suppression of secondary T_2 peaks, delay of characteristic *n*-alkane decrease, and increased *n*-alkane selectivity.

5. Acknowledgements

This work was carried out as a part of SUBPRO, a Research-based Innovation Centre within Subsea Production and Processing. The authors gratefully acknowledge the financial support from SUBPRO, which is financed by the Research Council of Norway, major industry partners and NTNU.

6. Acronyms

CPM = cross-polarized microscopy

DSC = differential scanning calorimetry

EVA = ethylene vinyl-acetate copolymer

GC/MS = gas chromatography coupled mass spectrometry

HPLC = high-performance liquid chromatography

HVLP = high volume low pressure

MAC = poly(maleic anhydride amide co-a-olefin)

MSD = mass spectrometer detector

NMR = nuclear magnetic resonance

PPD = pour point depressant

PE = polyethylene

PE-PEP = polyethylene poly(ethylene-propylene)

PE-PEB = polyethylene poly(ethylene-butene)

PTFE = polytetrafluoroethylene

TIC = total ion chromatogram

TGA = thermogravimetric analyzer

WAT = wax appearance temperature

WPC = wax precipitation curve

7. References

1. Huang, Z., S. Zheng, and H.S. Fogler, *Wax Deposition: Experimental Characterizations, Theoretical Modeling, and Field Practices*. 2015, Boca Raton (FL), USA: CRC Press.
2. Kelland, M.A., *Wax (Paraffin) Control*, in *Production Chemicals for the Oil and Gas Industry*. 2009, CRC Press.
3. Venkatesan, R., *The deposition and rheology of organic gels*. 2004, University of Michigan.
4. Sarica, C. and M. Volk, *Tulsa University Paraffin Deposition Projects*. 2004, The University of Tulsa (US). p. 130.
5. Singh, P.V., Ramachandran; Fogler, H. Scott; Nagarajan, Nagi, *Formation and aging of incipient thin film wax-oil gels.* AIChE Journal 2000. **45**(5): p. 1059-1074.
6. Yang, F., et al., *Polymeric Wax Inhibitors and Pour Point Depressants for Waxy Crude Oils: A Critical Review.* Journal of Dispersion Science and Technology, 2015. **36**(2): p. 213-225.
7. Oschmann, H.-J., *Das Kristallisationsverhalten von Paraffinen in Abhängigkeit von ihrer Zusammensetzung sowie seine Beeinflussung durch Paraffininhibitoren*, in *Fakultät für Bergbau, Hüttenwesen und Maschinenwesen*. 1998, Technische Universität Clausthal: Papierflieger.
8. Machado, A.L.d.C. and E.F. Lucas, *Poly(Ethylene-co-Vinyl Acetate) (EVA) Copolymers as Modifiers of Oil Wax Crystallization.* Petroleum Science and Technology, 1999. **17**(9-10): p. 1029-1041.
9. Paso, K., et al., *Paraffin Polydispersity Facilitates Mechanical Gelation.* Industrial & Engineering Chemistry Research, 2005. **44**(18): p. 7242-7254.
10. Clarke, E.W., *Crystal Types of Pure Hydrocarbons in the Paraffin Wax Range.* Industrial & Engineering Chemistry, 1951. **43**(11): p. 2526-2535.
11. Kané, M., et al., *Morphology of paraffin crystals in waxy crude oils cooled in quiescent conditions and under flow.* Fuel, 2003. **82**(2): p. 127-135.
12. Paso, K.G., *Comprehensive treatise on shut-in and restart of waxy oil pipelines.* Journal of Dispersion Science and Technology, 2014. **35**(8): p. 1060-1085.
13. Venkatesan, R., et al., *The strength of paraffin gels formed under static and flow conditions.* Chemical Engineering Science, 2005. **60**(13): p. 3587-3598.
14. Zhao, Y., *Shut in and Restart of Waxy Crude Oil Pipelines: Gelation, Rheology Model Development, and Application of Polymer/Ionic Liquid Based Additive*. 2013, Norges teknisk-naturvitenskapelige universitet (NTNU): Tondheim, Norway.
15. Bai, Y. and Q. Bai, *Subsea engineering handbook*. 2012, Waltham (MA), USA: Gulf Professional Publishing (Elsevier).
16. *Standard Test Method for Pour Point of Petroleum Products*, in *D97*. 2017: ASTM International.
17. Wei, B., *Recent advances on mitigating wax problem using polymeric wax crystal modifier.* Journal of Petroleum Exploration and Production Technology, 2015. **5**(4): p. 391-401.
18. Claudy, P., et al., *Interactions between n-alkanes and cloud point-cold filter plugging point depressants in a diesel fuel. A thermodynamic study.* Fuel, 1993. **72**(6): p. 821-827.
19. Li, Y., et al., *Influence of Asphaltene Polarity on Crystallization and Gelation of Waxy Oils.* Energy & Fuels, 2018. **32**(2): p. 1491-1497.
20. Lei, Y., S. Han, and J. Zhang, *Effect of the dispersion degree of asphaltene on wax deposition in crude oil under static conditions.* Fuel Processing Technology, 2016. **146**: p. 20-28.
21. Alcazar-Vara, L.A., J.A. Garcia-Martinez, and E. Buenrostro-Gonzalez, *Effect of asphaltenes on equilibrium and rheological properties of waxy model systems.* Fuel, 2012. **93**: p. 200-212.
22. Tinsley, J.F., et al., *Waxy Gels with Asphaltenes 1: Characterization of Precipitation, Gelation, Yield Stress, and Morphology.* Energy & Fuels, 2009. **23**(4): p. 2056-2064.

23. Oliveira, G.E., et al., *The Effect of Asphaltenes, Naphthenic Acids, and Polymeric Inhibitors on the Pour Point of Paraffins Solutions.* Journal of Dispersion Science and Technology, 2007. **28**(3): p. 349-356.
24. Venkatesan, R., et al., *The Effect of Asphaltenes on the Gelation of Waxy Oils.* Energy & Fuels, 2003. **17**(6): p. 1630-1640.
25. Prahl, U., *Isolierung erdölstämmiger Pour Point Depressants und Untersuchung ihrer Wirkungsweise in paraffinhaltigen Fluiden*, in *Fakultät für Bergbau, Hüttenwesen und Maschinenwesen*. 2001, Technische Universität Clausthal: Papierflieger.
26. Ariza-León, E., D.-R. Molina-Velasco, and A. Chaves-Guerrero, *Review of Studies on Asphaltene - Wax Interaction and the Effect thereof on Crystallization.* CT&F - Ciencia, Tecnología y Futuro, 2014. **5**: p. 39-53.
27. Kriz, P. and S.I. Andersen, *Effect of Asphaltenes on Crude Oil Wax Crystallization.* Energy & Fuels, 2005. **19**(3): p. 948-953.
28. Smith, P.B. and R.M.J. Ramsden, *The Prediction Of Oil Gelation In Submarine Pipelines And The Pressure Required For Restarting Flow*, in *SPE European Petroleum Conference*. 1978, Society of Petroleum Engineers: London, United Kingdom.
29. Kurniawan, M., et al., *Influence of Microcrystalline Wax on the Properties of Model Wax-Oil Gels.* Energy & Fuels, 2018. **32**(5): p. 5857-5867.
30. Tinsley, J.F., et al., *Waxy Gels with Asphaltenes 2: Use of Wax Control Polymers.* Energy & Fuels, 2009. **23**(4): p. 2065-2074.
31. Guo, X., et al., *Effect of Cooling Rate on Crystallization of Model Waxy Oils with Microcrystalline Poly(ethylene butene).* Energy & Fuels, 2006. **20**(1): p. 250-256.
32. Schwahn, D., et al., *Self-Assembling Behavior in Decane Solution of Potential Wax Crystal Nucleators Based on Poly(co-olefins).* Macromolecules, 2002. **35**(3): p. 861-870.
33. Machado, A.L.C. and E.F. Lucas, *Influence of ethylene-co-vinyl acetate copolymers on the flow properties of wax synthetic systems.* Journal of Applied Polymer Science, 2002. **85**(6): p. 1337-1348.
34. Chen, Z., et al., *A Study on the Interaction of Crude Oil Waxes With Polyacrylate Pour Point Depressants by Monte Carlo Simulation.* Petroleum Science and Technology, 2014. **32**(17): p. 2151-2157.
35. Wu, Y., et al., *Modified Maleic Anhydride Co-polymers as Pour-Point Depressants and Their Effects on Waxy Crude Oil Rheology.* Energy & Fuels, 2012. **26**(2): p. 995-1001.
36. Li, L., et al., *Improvement of oil flowability by assembly of comb-type copolymers with paraffin and asphaltene.* AIChE Journal, 2012. **58**(7): p. 2254-2261.
37. Wu, C., et al., *Molecular dynamics simulation guiding the improvement of EVA-type pour point depressant.* Fuel, 2005. **84**(16): p. 2039-2047.
38. Zhao, Z., et al., *A new kind of nanohybrid poly(tetradecyl methyl-acrylate)-graphene oxide as pour point depressant to evaluate the cold flow properties and exhaust gas emissions of diesel fuels.* Fuel, 2018. **216**: p. 818-825.
39. Yao, B., et al., *Performance improvement of the ethylene-vinyl acetate copolymer (EVA) pour point depressant by small dosage of the amino-functionalized polymethylsilsesquioxane (PAMSQ) microsphere.* Fuel, 2018. **220**: p. 167-176.
40. Jing, G., et al., *Influence of Different Vinyl Acetate Contents on the Properties of the Copolymer of Ethylene and Vinyl Acetate/Modified Nano-SiO2 Composite Pour-Point Depressant.* Energy & Fuels, 2017. **31**(6): p. 5854-5859.
41. Yao, B., et al., *Organically modified nano-clay facilitates pour point depressing activity of polyoctadecylacrylate.* Fuel, 2016. **166**: p. 96-105.
42. Song, X., et al., *Effect of SiO2 Nanoparticles on Wax Crystallization and Flow Behavior of Model Crude Oil.* Industrial & Engineering Chemistry Research, 2016. **55**(23): p. 6563-6568.
43. Norrman, J., et al., *Nanoparticles for Waxy Crudes: Effect of Polymer Coverage and the Effect on Wax Crystallization.* Energy & Fuels, 2016. **30**(6): p. 5108-5114.

44. Yang, F., et al., *Hydrophilic nanoparticles facilitate wax inhibition.* Energy & Fuels, 2015. **29**(3): p. 1368-1374.
45. Zhang, D., et al., *Application of Nano-Material Based Hybrid Pour-Point Depressant for Long-Distance Waxy Crude Pipeline.* 2012(45127): p. 459-466.
46. Zhao, Y., et al., *Utilization of DSC, NIR, and NMR for wax appearance temperature and chemical additive performance characterization.* Journal of Thermal Analysis and Calorimetry, 2015. **120**(2): p. 1427-1433.
47. Paso, K.G., et al., *PPD architecture development via polymer–crystal interaction assessment.* Journal of Petroleum Science and Engineering, 2014. **115**: p. 38-49.
48. Subramanian, S., et al., *Asphaltene fractionation based on adsorption onto calcium carbonate: Part 2. Self-association and aggregation properties.* Colloids and Surfaces A: Physicochemical and Engineering Aspects, 2017. **514**: p. 79-90.
49. Pinto, F.E., et al., *Fractionation of asphaltenes in n-hexane and on adsorption onto CaCO3 and characterization by ESI(+)FT-ICR MS: Part I.* Fuel, 2017. **210**: p. 790-802.
50. Subramanian, S., et al., *Asphaltene fractionation based on adsorption onto calcium carbonate: Part 1. Characterization of sub-fractions and QCM-D measurements.* Colloids and Surfaces A: Physicochemical and Engineering Aspects, 2016. **495**: p. 136-148.
51. Ruwoldt, J., M. Kurniawan, and H.-J. Oschmann, *Non-linear dependency of wax appearance temperature on cooling rate.* Journal of Petroleum Science and Engineering, 2018. **165**: p. 114-126.
52. Coto, B., et al., *Analysis of paraffin precipitation from petroleum mixtures by means of DSC: Iterative procedure considering solid–liquid equilibrium equations.* Fuel, 2010. **89**(5): p. 1087-1094.
53. Kruka, V.R., E.R. Cadena, and T.E. Long, *Cloud-Point Determination for Crude Oils.* Journal of Petroleum Technology, 1995. **47**(08): p. 681-687.
54. Roenningsen, H.P., et al., *Wax precipitation from North Sea crude oils: 1. Crystallization and dissolution temperatures, and Newtonian and non-Newtonian flow properties.* Energy & Fuels, 1991. **5**(6): p. 895-908.
55. Meiboom, S. and D. Gill, *Modified Spin-Echo Method for Measuring Nuclear Relaxation Times.* Review of Scientific Instruments, 1958. **29**(8): p. 688-691.
56. Provencher, S.W., *A constrained regularization method for inverting data represented by linear algebraic or integral equations.* Computer Physics Communications, 1982. **27**(3): p. 213-227.
57. Slichter, C.P., *Principles of magnetic resonance*. Vol. 1. 2013, Springer-Verlag Berlin Heidelberg: Springer Science & Business Media.
58. Zhao, Y., et al., *Gelation and Breakage Behavior of Model Wax–Oil Systems: Rheological Properties and Model Development.* Industrial & Engineering Chemistry Research, 2012. **51**(23): p. 8123-8133.
59. Ruwoldt, J., et al., *Asphaltene fractionation based on adsorption onto calcium carbonate: Part 3. Effect of asphaltenes on wax crystallization.* Colloids and Surfaces A: Physicochemical and Engineering Aspects, 2018. **554**: p. 129-141.
60. Jung, T., J.-N. Kim, and S.-P. Kang, *Influence of polymeric additives on paraffin wax crystallization in model oils.* Korean Journal of Chemical Engineering, 2016. **33**(6): p. 1813-1822.
61. Yi, S. and J. Zhang, *Relationship between Waxy Crude Oil Composition and Change in the Morphology and Structure of Wax Crystals Induced by Pour-Point-Depressant Beneficiation.* Energy & Fuels, 2011. **25**(4): p. 1686-1696.
62. Pedersen, K.S. and H.P. Rønningsen, *Influence of Wax Inhibitors on Wax Appearance Temperature, Pour Point, and Viscosity of Waxy Crude Oils.* Energy & Fuels, 2003. **17**(2): p. 321-328.

63. Jestin, J. and L. Barré, *Application of NMR Solvent Relaxation and SAXS to Asphaltenes Solutions Characterization.* Journal of Dispersion Science and Technology, 2004. **25**(3): p. 341-347.
64. Duval, F.P., et al., *An NMR Investigation of Water Self-Diffusion and Relaxation Rates in Controlled Ionic Strength Laponite Sols and Gels.* Journal of Colloid and Interface Science, 2001. **242**(2): p. 319-326.
65. Chen, W., Z. Zhao, and C. Yin, *The interaction of waxes with pour point depressants.* Fuel, 2010. **89**(5): p. 1127-1132.